JGR Solid Earth

RESEARCH ARTICLE
10.1029/2018JB016679

Origin and Transformation of Light Hydrocarbons Ascending at an Active Pockmark on Vestnesa Ridge, Arctic Ocean

T. Pape[1], S. Bünz[2], W.-L. Hong[2,3], M. E. Torres[4], M. Riedel[5], G. Panieri[2], A. Lepland[2,3], C.-W. Hsu[1], P. Wintersteller[1], K. Wallmann[5], C. Schmidt[5], H. Yao[2], and G. Bohrmann[1]

[1]MARUM—Center for Marine Environmental Sciences and Department of Geosciences, University of Bremen, Bremen, Germany, [2]Centre for Arctic Gas Hydrate, Environment and Climate, Department of Geosciences, UiT—The Arctic University of Norway, Tromsø, Norway, [3]Geological Survey of Norway, Trondheim, Norway, [4]College of Earth Ocean and Atmospheric Sciences, Oregon State University, Corvallis, OR, USA, [5]GEOMAR—Helmholtz Centre for Ocean Research, Kiel, Germany

Abstract We report on the geochemistry of hydrocarbons and pore waters down to 62.5 mbsf, collected by drilling with the MARUM-MeBo70 and by gravity coring at the Lunde pockmark in the Vestnesa Ridge. Our data document the origin and transformations of volatiles feeding gas emissions previously documented in this region. Gas hydrates are present where a fracture network beneath the pockmark focusses migration of thermogenic hydrocarbons characterized by their C_1/C_{2+} and stable isotopic compositions (δ^2H-CH_4, δ^{13}C-CH_4). Measured geothermal gradients (~80 °C/km) and known formation temperatures (>70 °C) suggest that those hydrocarbons are formed at depths >800 mbsf. A combined analytical/modeling approach, including concentration and isotopic mass balances, reveals that pockmark sediments experience diffuse migration of thermogenic hydrocarbons. However, at sites without channeled flow this appears to be limited to depths >~50 mbsf. At all sites we document a contribution of microbial methanogenesis to the overall carbon cycle that includes a component of secondary carbonate reduction—that is, reduction of dissolved inorganic carbon generated by anaerobic oxidation of methane in the uppermost methanogenic zone. Anaerobic oxidation of methane and carbonate reduction rates are spatially variable within the pockmark and are highest at high-flux sites. These reactions are revealed by ^{13}C depletions of dissolved inorganic carbon at the sulfate-methane interface at all sites. However, ^{13}C depletions of CH_4 are only observed at the low methane flux sites because changes in the isotopic composition of the overall methane pool are masked at high-flux sites. ^{13}C depletions of total organic carbon suggest that at seeps sites, methane-derived carbon is incorporated into de novo synthesized biomass.

Key Points:
- Drilling with the seafloor drill rig MeBo70 revealed two major hydrocarbon sources beneath a pockmark at the crest of Vestnesa Ridge
- Thermogenic methane likely formed at depths >800 m below seafloor ascends through faults and leads to hydrate formation and seafloor emission
- Methane is transformed into dissolved inorganic carbon at all sites investigated with highest rates observed at active seafloor emission sites

Supporting Information:
- Supporting Information S1
- Data Set S1

Correspondence to:
T. Pape,
tpape@marum.de

Citation:
Pape, T., Bünz, S., Hong, W.-L., Torres, M. E., Riedel, M., Panieri, G., et al. (2020). Origin and Transformation of Light Hydrocarbons Ascending at an Active Pockmark on Vestnesa Ridge, Arctic Ocean. *Journal of Geophysical Research: Solid Earth*, *125*, e2018JB016679. https://doi.org/10.1029/2018JB016679

Received 10 SEP 2018
Accepted 17 OCT 2019
Accepted article online 25 OCT 2019

1. Introduction

In marine sediments, light hydrocarbons are commonly formed via two well-known processes that can be distinguished by their molecular and compound-specific stable C and H isotopic compositions (Bernard et al., 1977; Whiticar, 1999). Microbial hydrocarbon production leads to a strong prevalence of methane (C_1/C_{2+} > approximately 1,000) depleted in ^{13}C (δ^{13}C-CH_4 less than approximately −55‰) due to kinetic fractionation (Rice & Claypool, 1981). This process is carried out by methanogenic archaea at temperatures below approximately 80 °C (Wilhelms et al., 2001), that is, at relatively shallow sediment depth. By contrast, thermogenic hydrocarbons are derived from the thermocatalytic decomposition of organic matter at temperatures exceeding approximately 70 °C (Hunt, 1996; Quigley & Mackenzie, 1988), that is, in sediments buried hundreds of meters below the seafloor. In addition to methane that is less depleted in ^{13}C (δ^{13}C-CH_4 > approximately −53‰; e.g., Clayton, 1991), thermogenesis also leads to production of significant amounts of higher hydrocarbons (C_1/C_{2+} < approximately 1,000).

Early diagenetic processes and biogeochemical modifications in shallow sediments drastically alter the properties of fluids ascending from greater depth. Upward-rising methane is oxidized by anaerobic and aerobic biological communities, limiting its escape to the water column (Boetius & Wenzhöfer, 2013). The anaerobic oxidation of methane (AOM) at the expense of seawater-derived sulfate is performed by a consortium of sulfate-reducing bacteria and methanotrophic archaea (Boetius et al., 2000) at the sulfate-methane

interface (SMI), while the aerobic oxidation of methane occurs in overlying, oxygenated sediments and in the water column. However, both processes increase the concentration of dissolved inorganic carbon (DIC). Previous studies have documented that the transformation efficiency of the AOM benthic filter depends on the rate and phase at which methane is delivered to the SMI, such that a higher portion of dissolved methane is able to escape the benthic filter at sites where the methane flux is high (Boetius & Wenzhöfer, 2013; Luff & Wallmann, 2003; Sommer et al., 2006). The benthic filter is also bypassed when methane is transported in the gas phase through faults and fractures. Due to isotope fractionations inherent in the various formation and transformation processes, both the origin and metabolic pathways of methane-derived carbon can be evaluated by stable carbon isotope analysis coupled with isotopic mass balance calculations (e.g., Heuer et al., 2009; Hong et al., 2013).

Vestnesa Ridge is a sediment drift characterized by the presence of gas at depth and by several gas-emitting pockmarks at the seafloor (e.g., Vogt et al., 1994); gas hydrate at this location has been mapped via a widespread bottom-simulating reflector (BSR). In the past, the ridge was investigated for its subsurface structures (Bünz et al., 2012; Hustoft et al., 2009; Plaza-Faverola et al., 2015, Plaza-Faverola et al., 2017), for the distribution and time variability of seafloor gas emissions (Bünz et al., 2012; Knies et al., 2018; Smith et al., 2014), and for the biogeochemistry of shallow pockmark-associated sediments (Hong et al., 2016; Panieri et al., 2017). Early diagenetic modifications affect the composition of shallow fluids and thus are not always representative of the fluid system at greater depth. However, because deep fluids have not been sampled to date, questions remain on the gas generation and migration processes within and outside pockmarks on Vestnesa Ridge. To address these questions we obtained cores to a depth of ~62 m below seafloor (mbsf) using the drill rig MARUM-MeBo70 (Freudenthal & Wefer, 2013) from areas within and outside the active Lunde pockmark in the eastern Vestnesa Ridge sector.

Sediment cores were sampled for their fluid composition at sites experiencing different modes of hydrocarbon transport and fluid flux rates. These data were complemented with numerical approaches that take advantage of state of the art knowledge of hydrocarbon generation and cycling of hydrocarbon-derived carbon to (i) determine formation processes and source depth of the hydrocarbons fueling shallow hydrate deposits and seafloor gas emissions at pockmarks, (ii) evaluate the role of pockmark-associated faults as gas migration pathways, and (iii) characterize microbial methane transformation as an important component of the carbon cycle in these sediments.

2. Geological Setting

Vestnesa Ridge (Figures 1a–1g) is a 100-km-long submarine sediment drift located along the west Svalbard margin (Arctic Ocean), at water depths between approximately 1,200 and 1,500 m below sealevel (mbsl; Crane et al., 1991; Hustoft et al., 2009; Petersen et al., 2010; Plaza-Faverola et al., 2015; Plaza-Faverola et al., 2017; Ritzmann et al., 2004; Vogt et al., 1994). The ridge hosts a sedimentary succession that reaches up to 5 km in thickness in its southeastern segment (Eiken & Hinz, 1993; Ritzmann et al., 2004). Syn- and post-rift deposits of Miocene age that lie above a relatively young (<20 Ma) and hot oceanic crust are overlain by a contourite sequence that extends to the onset of the Plio-Pleistocene glaciations at ~2.7 Ma; a horizon that corresponds to a regional unconformity throughout the Fram Strait (Eiken & Hinz, 1993; Engen et al., 2008; Hustoft et al., 2009; Knies et al., 2009). The youngest sediments at Vestnesa Ridge are primarily comprised of silty turbidites and muddy-silty contourites with abundant ice-rafted debris from late Weichselian to Holocene in age (Howe et al., 2008; Knies et al., 2009; Knies et al., 2014; Mattingsdal et al., 2014; Schneider et al., 2018).

The deep water gas hydrate and gas discharge systems on Vestnesa Ridge have been previously documented (Fisher et al., 2011; Graves et al., 2017; Panieri et al., 2017; Smith et al., 2014) and are thought to be affected by heat flow changes associated with the underlying ultraslow-spreading Molloy Ridge (Bünz et al., 2012; Crane et al., 1991; Smith et al., 2014; Vanneste et al., 2005). The base of the gas hydrate stability zone (GHSZ) has been inferred by a prominent BSR in this area, mapped at about 160–195 mbsf (Bünz et al., 2012; Dumke et al., 2016; Hustoft et al., 2009; Petersen et al., 2010; Plaza-Faverola et al., 2015; Plaza-Faverola et al., 2017; Smith et al., 2014). High-resolution seismic data have been used to identify accumulations of free gas below the base of the GHSZ. A network of near-vertical faults and fractures and abundant acoustic chimney structures that stretch from below the BSR towards the seafloor are imaged in the seismic

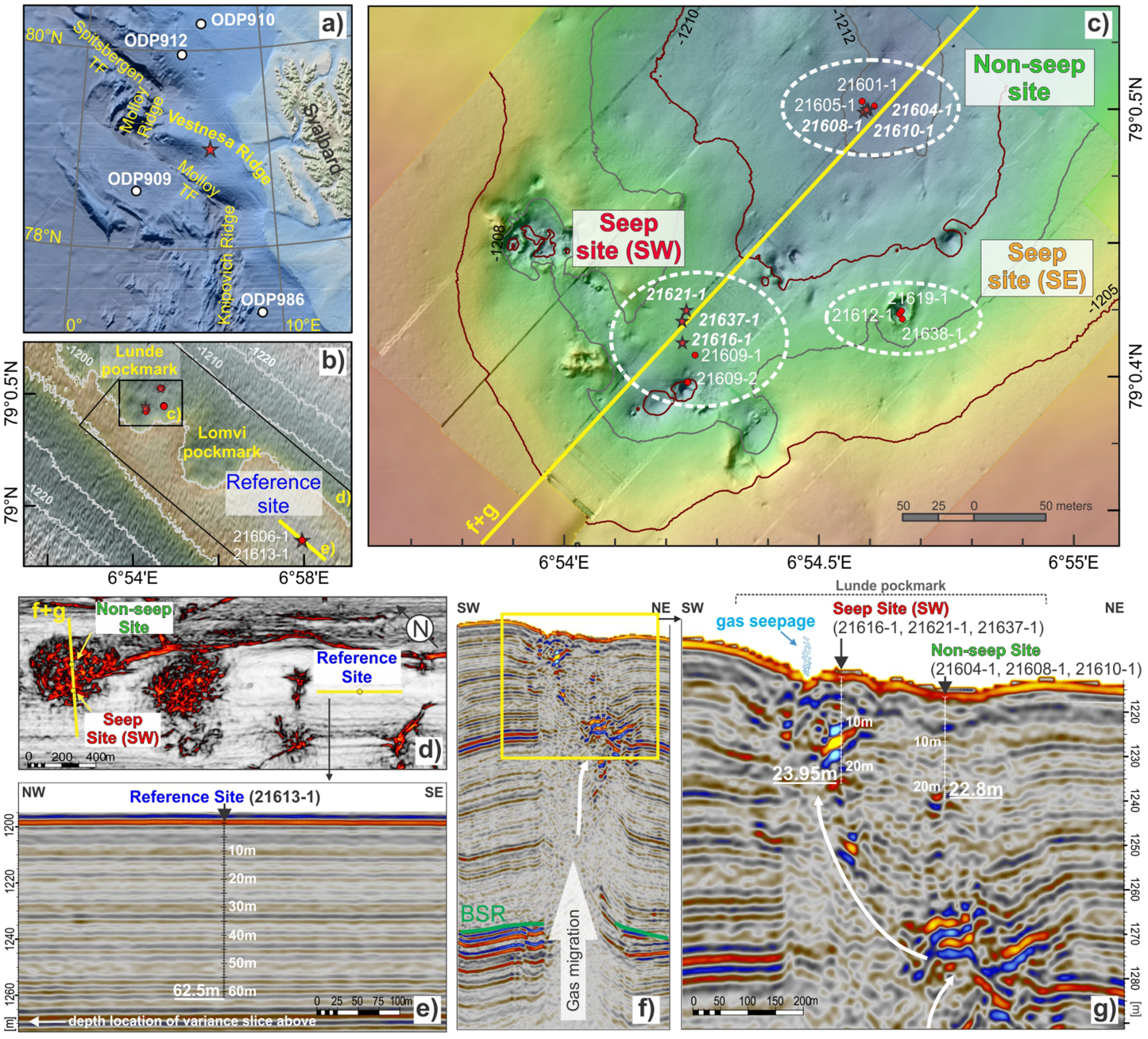

Figure 1. (a) Bathymetric map of the eastern Fram Strait showing the position of Vestnesa Ridge west off Svalbard relative the slow-spreading Molloy Ridge and the Molloy Transform Fault (TF = Transform Fault). Data source: GMRT (Ryan et al., 2009). Red star shows position of the working area on the eastern segment of the Vestnesa Ridge comprising active pockmarks. Positions of ODP drilling Sites 912, 909, 910, and 986 are shown. (b) Bathymetry of the SE Vestnesa Ridge indicating positions of Lunde and Lomvi pockmarks and of the reference station. For maps showing positions of additional cores published in previous studies see Figure S2 in the supporting information. (c) Micro-bathymetric map of Lunde pockmark showing positions of gravity cores and MeBo cores at the nonseep site and the two seep sites. For additional information on hydroacoustic mapping refer to Text S1 in the supporting information. (d–g) High-resolution 3D seismic data along the crest of Vestnesa Ridge (NW-SE direction; P cable 3D (Bünz, 2013) covering MeBo drill sites that were selected as a reference site outside any leakage structure (e) as indicated by the variance map (d; see also Plaza-Faverola et al., 2015) and over Lunde pockmark and associated chimney beneath (SW-NE direction) covering the nonseep site and the seep site in the southwest of the pockmark (f, g). Note: A BSR was present at all sites at approximately 195 mbsf (Bünz et al., 2012; Plaza-Faverola et al., 2017).

data and reveal a system of channeled fluid migration pathways feeding the observed gas discharge at the seafloor (Bünz et al., 2012; Hustoft et al., 2009; Plaza-Faverola et al., 2015; Smith et al., 2014). Recently, a microfracture array has been shown to serve as a conduit for the fast-ascending methane gas that impacts the microbial community in the near-seafloor sediments (Yao et al., 2019).

Numerous pockmarks forming semicircular seafloor depressions, as large as 800 m in diameter and tens of meters in vertical relief, occur above chimney structures and align the crest of Vestnesa Ridge (Bünz et al., 2012; Hustoft et al., 2009; Panieri et al., 2017; Petersen et al., 2010; Vogt et al., 1994). Episodic seepage of gas at the seafloor, imaged as hydroacoustic anomalies in the water column, has been repeatedly documented as emanating from individual pits within the pockmarks at the southeastern segment of the ridge (Bünz et al., 2012; Hustoft et al., 2009; Panieri et al., 2017; Smith et al., 2014). A series of paleo methane proxies have been used to postulate that episodic methane discharge events have been occurring in this region over the past 23,500 years BP (Ambrose et al., 2015; Panieri et al., 2014; Schneider et al., 2018; Sztybor & Rasmussen, 2017a). These events have been attributed to changes in tectonic stress and/or glacioeustatic forcings and are thought to have caused the current pockmark distribution on the seafloor (Bünz et al., 2012; Petersen et al., 2010; Plaza-Faverola et al., 2015; Plaza-Faverola & Keiding, 2019; Vogt et al., 1994; Vogt et al., 1999). Analyses of gas hydrate recovered from shallow deposits of Lunde and the nearby Lomvi pockmarks generally indicate a deep thermogenic hydrocarbon source (Fisher et al., 2011; Graves et al., 2017; Panieri et al., 2017; Smith et al., 2014); however, data from several shallow sediment cores point to a mixture of thermogenic hydrocarbons and microbial methane produced in shallow sediment (Panieri et al., 2017).

Crusts of authigenic seep carbonates have a patchy distribution on the seabed in both, the Lunde and Lomvi pockmarks. They occupy approximately 15% of the pockmark area, with individual carbonate patches having diameters of up to 50 m (Panieri et al., 2017). Subsurface carbonate crusts were recovered during expeditions MSM57-1 and MSM57-2 with the MARUM-MeBo-70 from a seep site that targeted the carbonate patches in the southwestern sector of the Lunde pockmark (GeoB21616-1 and GeoB21637-1 in Figures 1 and 2; Himmler et al., 2019). Calcium carbonate abundance of >75% is reported in discrete depth intervals between 5 and 22 mbsf, with aragonite being the dominating mineralogical phase (Himmler et al., 2019). Aragonitic crusts, as reported by Himmler et al. (2019), are thought to form under high methane flux conditions, when the SMI is situated very close to the sediment-water interface (Aloisi et al., 2002; Luff & Wallmann, 2003). The SMI at this site is currently located at ~1 mbsf, so Himmler et al. (2019) interpret the subsurface crusts as indicative of past high methane emission episodes, when the SMI was situated close to the sediment-water interface.

3. Materials and Methods

3.1. Core Sampling

During expeditions MSM57-1 and MSM57-2 in 2016, we sampled sediment from the Lunde pockmark and its vicinity to a depth of 62.5 mbsf with the seafloor drill rig MARUM-MeBo70 (Freudenthal & Wefer, 2013). From the three deployments of the MeBo pressure core system MDP (MeBo-Druckkern-Probennehmer; Pape et al., 2017) two were recovered at full in situ pressure. The MeBo conventional and pressurized cores were complemented with several gravity cores up to 7.7 m in length (Figures 1b, 1c, 1e, 1g, and 2 and Table S1 in the supporting information).

Anomalous amplitudes and chaotic reflection geometry beneath Lunde pockmark are interpreted as gas migration pathways leading to gas seepage from pits at the seafloor (Figures 1f and 1g; Bünz, 2013; Panieri et al., 2017; Plaza-Faverola et al., 2015). We collected sediment from the perimeter of two individual seafloor sites in the southern sector of the Lunde pockmark, where seafloor gas seepage was observed in agreement with previous surveys in the area (Panieri et al., 2017) and denote these as seep site southwest (SW) and seep site southeast (SE). A nonseep site within the Lunde pockmark, which did not show any indication of seafloor gas release, was also sampled. In addition, a site approximately 8 km away from the SE pockmark (Figures 1b, 1d, and 1e) was used as a reference. Here seismic data indicate the subseafloor to be characterized by a homogenous series of nearly undisturbed sediments with no indication of fluid or gas seepage (Figure 1e; Plaza-Faverola et al., 2015).

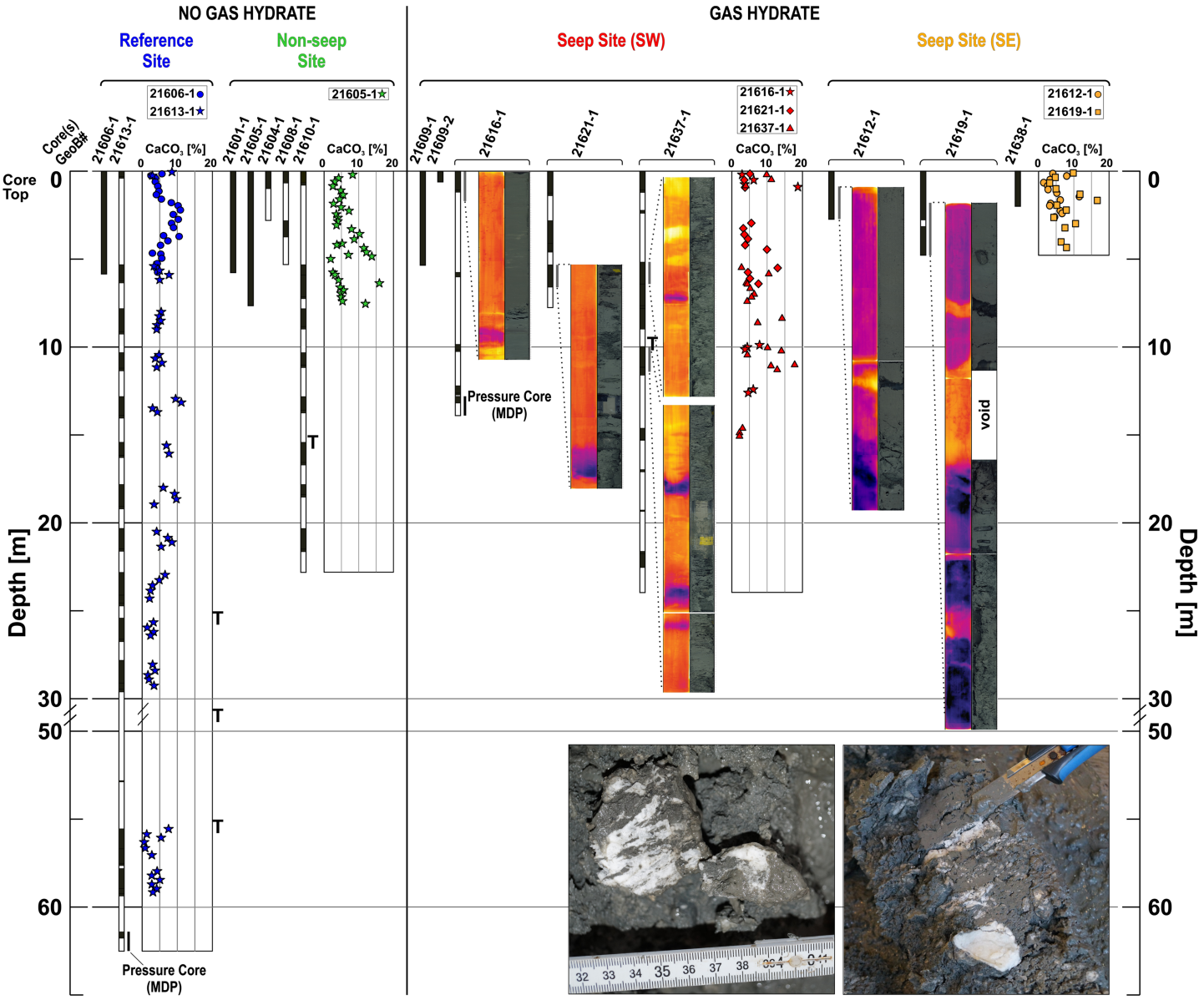

Figure 2. Overview of gravity cores and MeBo cores from the study sites at Vestnesa Ridge. Core recoveries of individual MeBo and gravity cores shown in bar diagrams with recovered sediment depths depicted as black fields and voids as white fields. Total core lengths and total core recoveries given in Table S1 in the supporting information. Borehole depths of pressure cores indicated by black vertical bars to the right of core recoveries. For gas hydrate-bearing sites, depth ranges of infrared images and photographs shown for hydrate-bearing sediment intervals are indicated by gray vertical bars to the right of core recoveries. Carbonate ($CaCO_3$) contents (wt.%) versus depth jointly illustrated for cores with available $CaCO_3$ data (gravity cores = circles, squares; MeBo cores = stars, diamonds, triangles) from each site. Lengths of graphs showing site-specific $CaCO_3$ contents correspond to longest cores from each site. T = Depth of in situ sediment temperature measurement. Photographs and infrared images of such core segments that showed relative cooling due to endothermic hydrate dissociation in cores from the seep sites. Temperature color codes not normalized; yellow = warm, blue = cold. Note: Photographs and core infrared images do not correspond to depth scale. Pictures of hydrates pieces recovered with core GeoB21619-1 (scale: centimeters).

3.2. Core Infrared Scanning and Imaging

MeBo core liners (2.52 m long) and gravity cores (1-m whole round segments) were scanned with an infrared (IR) camera (ThermaCam SC 640 camera, FLIR Systems) immediately after recovery to document gas hydrate occurrence, following the method described by Wei et al. (2015). Detectable temperatures of the IR camera range from −40 °C to +120 °C with a precision of ±2 °C and an accuracy of 0.1 °C at 30 °C.

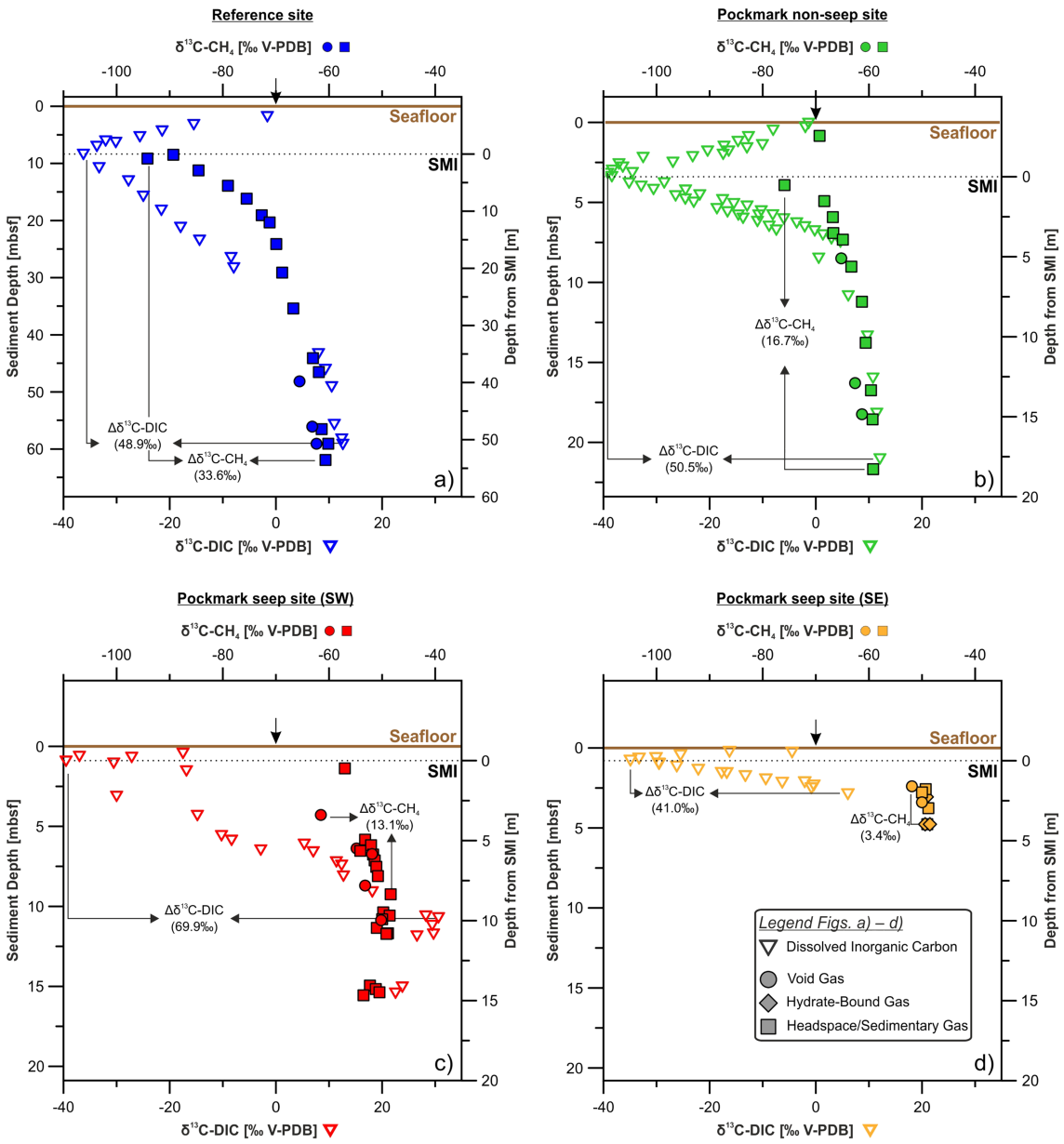

Figure 3. δ^{13}C-DIC (open triangles, bottom x-axis) and δ^{13}C-CH_4 in various gas types (closed symbols, top x-axis) versus depth at the four sites investigated on the Vestnesa Ridge. (a) Reference site. (b) Nonseep site. (c) Seep site SW. (d) Seep site SE. A decoupling of pore water DIC from methane is apparent at the high-flux sites. Black vertical arrows at the top axis illustrate δ^{13}C values of seawater DIC (0‰ VPDB). Note different scaling of depth axis in Figure 3a.

For the MeBo cores, each thermal scan of the core liners covered approximately 60 cm; five to six scans including a spatial overlap of about 10 cm were taken from each liner in less than 1 min. From each drilling/coring station, all IR images were merged to illustrate temperature variations along the entire cored depth (Figure 2).

Following the IR scans, all core sections were split lengthwise. The archive halves were used for high-resolution imaging (Figure 2), using the SmartCIS 1600LS line scanning system of the MARUM GeoB Core repository at a 500-dpi resolution (www.marum.de/en/Infrastructure/GeoB-smartCIS-1600-Line-Scanner.html). The archive halves were then described onboard while the working half of each core was sampled as described below.

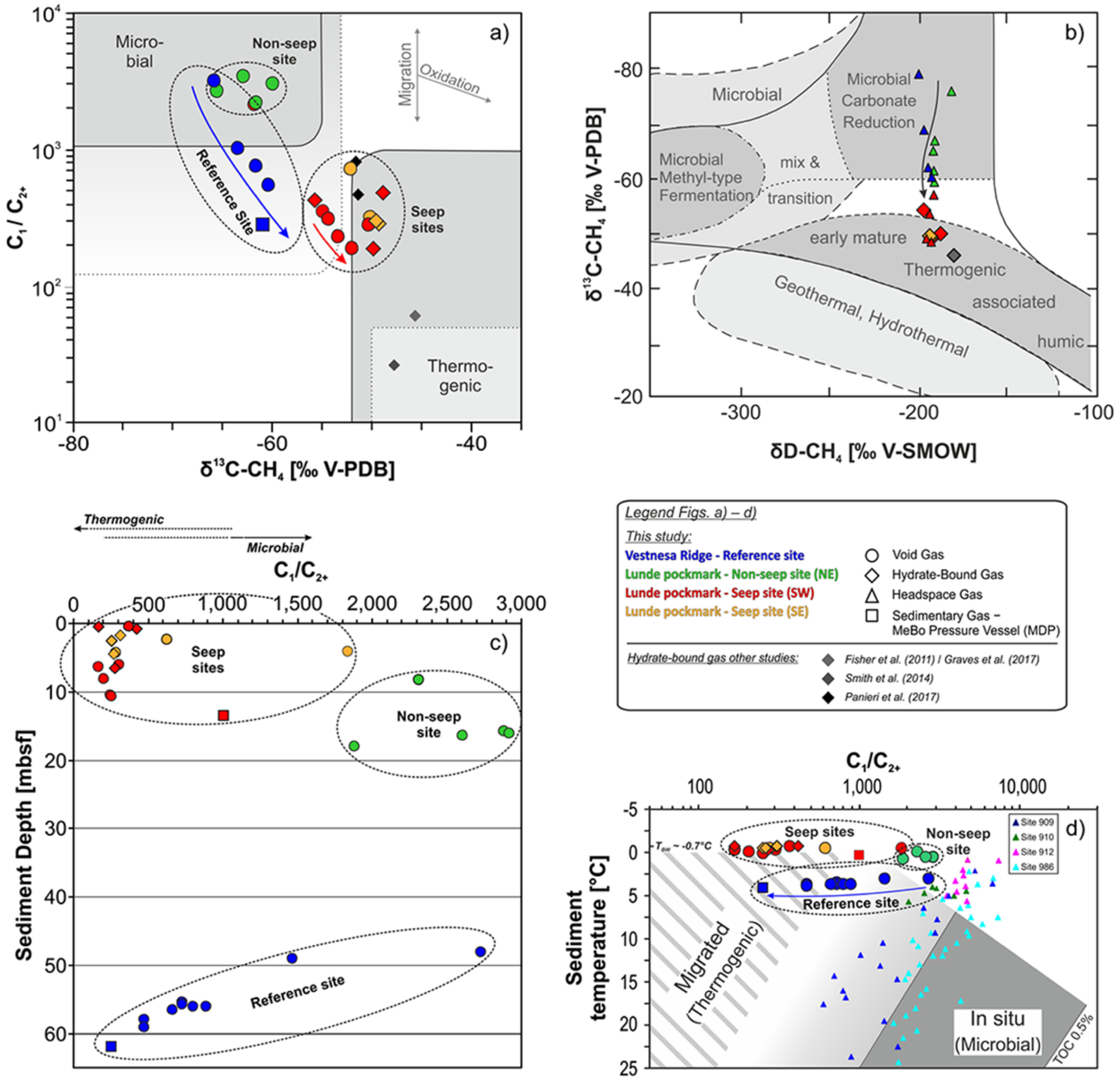

Figure 4. (a) Relationship between molecular composition of light hydrocarbons (expressed as C_1/C_{2+}) and stable carbon isotopic composition of methane ($\delta^{13}C$-CH_4) in various gas types prepared from MeBo cores. Extents of fields assigned for microbial and thermogenic light hydrocarbons according to Bernard et al. (1977; dark gray) and Whiticar (1999; light gray). Considering classifications proposed by Bernard et al. (1977) hydrocarbons in most hydrate samples recovered from seep sites within Lunde pockmark plot within the field representative for thermogenic hydrocarbons. All void gas samples recovered from the nonseep site at Lunde pockmark plot within the microbial field. Directions of arrows close to samples from individual sites indicate increasing sediment depth. Specifics of methane bound in shallow hydrates from Lunde pockmark (Fisher et al., 2011; Graves et al., 2017; Smith et al., 2014) and the adjacent Lomvi pockmark (Panieri et al., 2017) are shown for comparison. (b) δ^2H-$\delta^{13}C$ relationships of hydrate-bound methane collected at the seep sites and headspace gas from the reference site, the nonseep site and the SW seep site. Classification according to Whiticar (1999). Specifics of methane bound in shallow hydrate from Lunde pockmark (*core JR211-26-GC;* Fisher et al., 2011; Graves et al., 2017) is shown for comparison. Note: Arrow illustrates increasing depth for headspace samples (triangles) from the reference site, the nonseep site and the seep site SW collected from ~1.0 to 59.1 mbsf. Maximum burial depth of hydrates analyzed (diamonds) is ~6.6 mbsf. (c) C_1/C_{2+} ratios in various gas types versus sediment depth from multiple cores at the seep sites, at the nonseep site, and at the reference site, respectively. Assignments of thermogenic and microbial hydrocarbon sources based on C_1/C_{2+} ratios according to Bernard et al. (1977) and Whiticar (1999). (d) Relationship between C_1/C_{2+} ratios and sediment temperature at sites explored at the Vestnesa Ridge. Most of the samples from the seep sites and deepest samples from the reference site plot within the field representative for migrated thermogenic hydrocarbons. Samples from the nonseep site within the pockmark plot close to or within the field assigned for light hydrocarbons produced in situ. For comparison, relationships at ODP drill sites explored during Legs 151 and 162 in the Fram Strait (Site 909), on the southern Yermak Plateau (Sites 910 and 912), and on the Svalbard Margin (Site 986) are shown as well (Shipboard Scientific Party, 1996; Stein et al., 1995). Direction of arrow close to samples from the reference site indicates increasing sediment depth. Figure modified after Stein et al. (1995). For calculation of in situ sediment temperatures, equations provided in Bohrmann et al. (2017) for sites within Lunde pockmark (T [°C] = 0.0813 [°C/m] × z [m] – 0.6822 [°C]) and the reference site (T [°C] = 0.0777 [°C/m] × z [m] – 0.6822 [°C]) were used.

3.3. Sampling Procedures

3.3.1. Gas Sampling

Hydrate-bound gas, gas from expansion voids ("void gas"), and sedimentary gas were obtained from five MeBo cores and seven gravity cores (Tables S1 and S2 in the supporting information). For vertical profiling of ex situ concentrations of dissolved methane (i.e., in samples collected shortly after recovery under ambient P and T conditions) in the nonpressurized MeBo and gravity cores, we used a modified headspace technique after Kvenvolden and McDonald (1986), as described in Pape et al. (2014). Headspace samples were collected from the lowermost part of each MeBo core liner immediately after removal of the pilot chuck and the core catcher (2.5-m vertical resolution), that is, before the concentrations of light hydrocarbons had fully equilibrated to atmospheric pressure. For gravity cores in rigid polyvinyl chloride liners, samples were taken from the surface of freshly cut core whole rounds (1-m vertical resolution) before IR imaging. Additional samples were collected from selected depth intervals (25- to 50-cm distance) after core splitting. In all cases, 3 ml of bulk sediment was collected with cut-off syringes and transferred into 20-ml glass vials prefilled with 5 ml of 1-M NaOH.

Gas from expansion voids caused by exsolution from pore water dissolved gas (void gas) was collected from MeBo cores for analysis of its molecular composition. For sampling, a butyl rubber septum was placed on the transparent liner and holes of 1 mm in diameter were drilled through the septum into the liner, thereby minimizing escape of void gas and/or inflow of air from/to the liner. Gas was obtained by inserting a cannula attached to a plastic syringe through the septum into the core liner.

Hydrate-bound gas was prepared from hydrate pieces according to Pape et al. (2010). Samples from both gas voids and gas hydrate were collected in glass serum vials prefilled with saturated NaCl solution for onboard analysis of its molecular composition and for determination of the methane stable carbon isotope compositions onshore (section 3.4.1).

Sedimentary gas was also obtained at stations GeoB21613-1 and GeoB21616-1 via controlled degassing of pressurized deep sediments collected with the MDP (Pape et al., 2017). For core degassing, we used an assembly of gas-tight valves and ports modified after Dickens et al. (2003) and a pressure sensor for continuous monitoring of the internal pressure in the MDP pressure chamber. Pressurized fluid (gas and water) was released incrementally into a gas-tight syringe for the collection of gas subsamples at preselected intervals, which were transferred into glass serum vials for analysis of hydrocarbon molecular and stable isotopic compositions.

3.3.2. Sediment and Pore Water Sampling

About 5 ml of wet sediment were collected at selected depth intervals to determine the sediment porosity, the total carbon (TC) and total organic carbon (TOC) concentrations, and the stable carbon isotope signatures of organic carbon (δ^{13}C-TOC). Pore water was collected routinely from MeBo sediment cores using a pressure (1–5 bar) filtration (0.2 μm) system at approximately 4 °C (e.g., Wallmann et al., 2018). In addition, pore water from gravity cores was extracted with rhizon soil moisture samplers (Seeberg-Elverfeldt et al., 2005). Fluid subsamples were poisoned with $HgCl_2$ onboard for shore-based characterization of the carbon isotope signatures of DIC (δ^{13}C-DIC). Subsamples for sulfate, calcium, and magnesium concentrations were preserved onboard as detailed in Wallmann et al. (2018). Titration of total alkalinity was performed 30–45 min after the extraction of pore fluid (see Bohrmann et al., 2017).

3.4. Analytical Methods

3.4.1. Hydrocarbon Analyses

All gas samples were analyzed onboard by gas chromatography (GC; Agilent Technologies; 6890N; Pape et al., 2010). Samples prepared according to the headspace technique yielded relatively low hydrocarbon concentrations and were used only for profiling of methane concentration, whereas hydrate-bound gas, void gas, and sedimentary gas from the MDP allowed for quantification of C_1 to C_6 hydrocarbons and for calculation of molecular hydrocarbon composition (C_1/C_{2+} ratios).

For molecular characterization, light hydrocarbons (C_1 to C_6) were separated, detected, and quantified with a capillary column connected to a flame ionization detector, while O_2, N_2, and CO_2 as well as C_1 and C_2 hydrocarbons were determined using a stainless-steel column packed with molecular sieve and coupled to a thermal conductivity detector. Calibration and performance checks of the analytical system were

conducted regularly using commercial pure gas standards and gas mixtures. The coefficient of variation determined for the analytical procedure is lower than 2%.

Stable carbon and hydrogen isotope ratios ($^{13}C/^{12}C$ and $^{2}H/^{1}H$) of methane in void gas, hydrate-bound gas, headspace gas, and sedimentary gas were determined by GC-isotope ratio mass spectrometry on gas aliquots characterized by elevated (greater than approximately 25,000 ppm) methane concentrations at the MARUM. For this, a Trace GC Ultra-GC IsoLink connected to a MAT 253 isotope ratio mass spectrometer via a ConFlo IV interface (all components Thermo Fisher Scientific Inc.) was used. Methane was separated by GC (CARBOXEN-1006 PLOT capillary column [Supelco Inc.]) and either combusted (1,030 °C) or pyrolized (1,440 °C) in order to generate CO_2 or H_2, respectively. CO_2 or H_2 were then transferred to the isotope ratio mass spectrometer for analysis of $^{13}C/^{12}C$ or $^{2}H/^{1}H$. All samples were injected at room temperature either manually or by use of a TriPlus RSH autosampler. Reported isotope ratios are arithmetic means of duplicate or triplicate measurements in the δ notation relative to Vienna Pee Dee Belemnite (VPDB) and Vienna Standard Mean Ocean Water (VSMOW; for carbon and hydrogen, respectively). Reproducibility was checked daily using commercial methane standards (Isometric Instruments, Canada; Air Liquide GmbH, Germany). Standard deviations of triplicate stable isotope measurements were <0.5‰ ($\delta^{13}C\text{-}CH_4$). Selected samples of hydrate-bound gas were additionally analyzed for $\delta^{2}H\text{-}CH_4$ at GEO-data Gesellschaft für Logging-Service mbH, Germany (Table S7 in the supporting information).

3.4.2. Analysis of Sediment Physical Properties

In addition to core imaging described above, the sediment cores were described onboard. Protocols for sediment description and curation are given in Bohrmann et al. (2017). For the determination of sediment porosity in discrete samples, sediment samples were taken on board as soon as possible after core recovery to minimize moisture loss. Sediment porosities were determined as described in Text S3 in the supporting information.

3.4.3. Analysis of Sediment Carbon Contents

Contents of TC and TOC of bulk sediment samples were determined with an elemental analyzer (vario EL III; Elementar, Germany) at MARUM as described in Text S4 in the supporting information. Briefly, aliquots of lyophilized and homogenized sediment samples were wrapped in tin capsules, weighed, and subject to catalytic combustion (950 °C, CuO, CeO_2, and $PbCrO_4$) with the addition of molecular oxygen. For the determination of TOC contents, sediment subsamples were weighed, treated with HCl (10%) for removal of carbonate carbon, rinsed with deionized water, dried, weighed (for determination of bulk inorganic carbon and nitrogen), homogenized, transferred into tin capsules, and reweighed. The acid-treated sediment samples were then subject to catalytic combustion as described above. The relative standard deviation for the carbon analyses as determined for replicate measurements of a house standard was <0.05%. Assuming all inorganic carbon was present as calcium carbonate, the $CaCO_3$ content was calculated as follows: $CaCO_3 = (TC - TOC) \times 8.333$. $\delta^{13}C\text{-}C_{org}$ was analyzed as described in Text S4 in the supporting information.

3.4.4. Pore Water Analysis

Concentrations of sulfate (SO_4^{2-}) were determined by ion chromatography (Metrohm, 861 Advanced Compact IC) at GEOMAR. Standard seawater from the International Association for Physical Sciences of Oceans was used for calibrating the system. Estimated accuracies of calculated concentrations were within ±3%.

Subsamples collected at sea for the stable carbon isotopic compositions of DIC were analyzed at Oregon State University using a GasBench II automated sampler interfaced to a stable isotope mass spectrometer (Finnigan DELTA Plus XL; Torres et al., 2005). $^{13}C/^{12}C$ values are reported in the δ notation relative to VPDB. The overall precision and accuracy are estimated to be better than ±0.15‰. Primary standardization is provided by tank CO_2 (referenced to an array of international standards) and analyses are monitored against a stock solution of reagent $NaHCO_3$.

3.5. Numerical Model

We used the stable carbon isotopic mass balance model developed by Hong et al. (2013) to quantify carbon cycle pathways among organic matter, DIC, and methane. A similar simulation approach was applied successfully at two other case studies (Chen et al., 2017; Crémière et al., 2017). Comparison showed that results derived from this box model approach are very similar to those from a more sophisticated transport-reaction

model (Hong et al., 2014). The three-box model describes the carbon exchanges across the SMI box, the seafloor, and sediments at greater depths. Mass balances of ^{12}C and ^{13}C were both considered to satisfy the isotopic constraints, including the stable carbon isotopic signatures of DIC, methane, and organic matter. The model considers the following reactions: AOM, carbonate precipitation (CP), organic matter degradation via methanogenesis (ME) and organoclastic sulfate reduction (POCSR), and a secondary CO_2 reduction (CR), whereby the DIC produced by AOM is further reduced to methane (see Figure 5a for the schematic diagram for the box model). The fundamental relationship that links reaction rates with the fluxes with respect to DIC is

$$\Delta F_{DIC} = \Sigma R\ (R_{AOM} + R_{ME} + R_{POCSR} - R_{CR} - R_{CP}) = F_{DIC-aboveSMI} + F_{DIC-belowSMI} \quad (1)$$

where F and R denote the fluxes and depth-integrated rates. We note that, based on the alkalinity profiles from all sites, $F_{DIC\text{-}aboveSMI}$ and $F_{DIC\text{-}belowSMI}$ have opposite signs. The only exception is the seep site SE, which has very low $F_{DIC\text{-}belowSMI}$ as alkalinity does not change significantly with depth below SMI. We can therefore define ΔF_{DIC} as the difference between the absolute fluxes of DIC below and above SMI, which we use later to compare with the reaction rates derived from our mass balance calculation. The modeling was done with the software program MS Excel; model, detailed equations, input parameters, and a description of the assumptions used can be found in Text S5 and Table S3 in the supporting information. The excel file for the calculation can be found as additional supporting information (Data Set S1).

4. Results

4.1. Sediment Characterization and Occurrences of Gas Hydrates

Sediments from all investigated sites were predominantly comprised of homogeneous silty clay and pebbly silty clay with intervals rich in ice-rafted debris and occasional isolated clasts. This composition is similar to that of sediments previously described for cores from nearby sites within the Lunde and the adjacent Lomvi pockmarks and sediments outside the pockmarks (Hong et al., 2016; Schneider et al., 2018; Sztybor & Rasmussen, 2017a). Porosities of the near-surface sediments ranged between 0.7 and 0.8 at all sites (Figure S3 in the supporting information). At the reference and the nonseep sites within the Lunde pockmark, porosity generally decreased with depth and reached values ranging between 0.45 and 0.55 at ~60 mbsf at the reference site. A much higher variability in porosity values (approximately 0.4 to 0.8) was obtained for sediments recovered from the seep sites (maximum sampling depth 15 and 5 mbsf, respectively). Mean carbonate ($CaCO_3$) contents were lowest at the reference site (5.1%; Figure 2), followed by the nonseep site (6.2%), seep site SW (6.8%), and seep site SE (6.3%). At the reference site, trends of carbonate contents in the uppermost approximately 5 m resembled those previously published for cores from a nearby site and from the Lomvi pockmark (Sztybor & Rasmussen, 2017b). Carbonate nodules were not found in the drilled sediments from the reference site (Bohrmann et al., 2017), whereas authigenic seep carbonates were present at the seafloor and in MeBo cores from the seep site SW, which have been described in detail by Himmler et al. (2019). Mean contents of TOC were 0.8 wt.% at both the reference and nonseep site, and 0.9 and 1.0 wt.% at the seep sites (Figure S4 and Table S6 in the supporting information).

Infrared scanning of core liners immediately after recovery revealed nearly uniform temperatures for all cores from the reference and nonseep site. In contrast, significant negative temperature anomalies ($\Delta T >$ 1 °C), indicative for endothermic dissociation of gas hydrates due to pressure reduction and temperature elevation, was observed in cores from the seep sites (Figure 2). For those cores, sediment surface cooling indicated the presence of gas hydrates at various depths down to approximately 11.2 mbsf. The shallowest gas hydrates in gravity cores were found at approximately 45 cmbsf at seep site SW (GeoB21609-1) and at seep site SE at approximately 232 cmbsf and approximately 330 cmbsf in cores GeoB21612 and GeoB21619-1, respectively. Gas hydrate appeared as pieces up to 5 cm thick or as layers up to several centimeters in thickness (Figure 2).

4.2. Pore Water Sulfate, DIC Isotopic Composition, and Methane Concentrations

Concentration profiles of dissolved methane in concert with sulfate concentrations and $\delta^{13}C$-DIC profiles were used to identify the depth of the site-specific SMI (Figure 3 and Figure S6 in the supporting

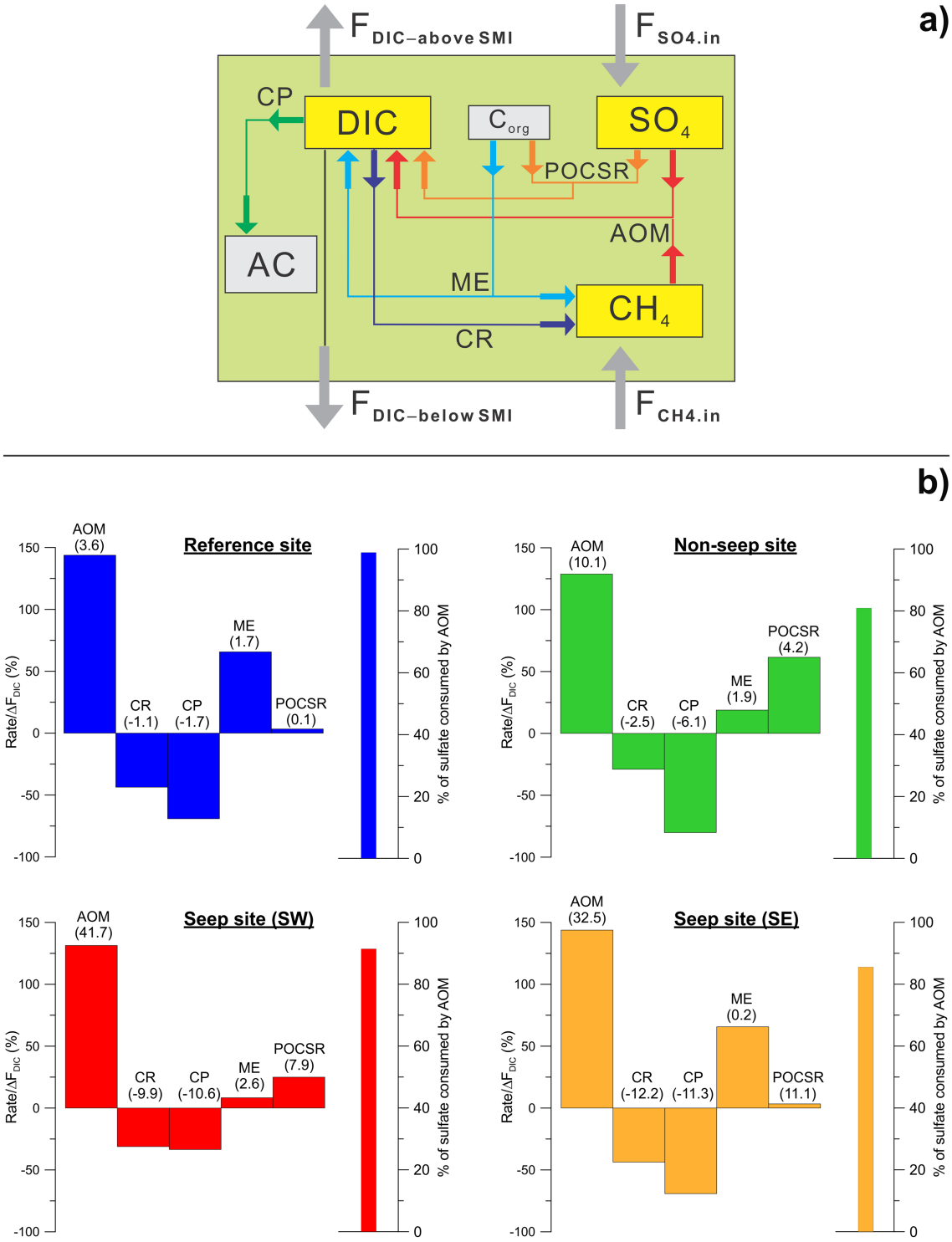

Figure 5. (a) Framework of box model used for evaluating the carbon cycling pathways. AOM = anaerobic oxidation of methane; CP = carbonate precipitation leading to formation of authigenic carbonate (AC); ME = organic matter degradation via methanogenesis; POCSR = organoclastic sulfate reduction, CR = secondary CO_2 reduction. (b) Histogram showing the relative contribution of each reaction responsible for DIC production/consumption. The height of the bars shows the relative contribution (in percentage) of each reaction with respect to the overall DIC flux (equation (1)). Numbers in parentheses are depth-integrated rates ($\mu mol \times cm^{-2} \times year^{-1}$).

information). Most of the MeBo cores had evidence of seawater contamination at depth, as indicated in erratic profiles with elevated sulfate below the SMI. Data collected using rhizons from the gravity cores are more reliable and better suited to define the SMI depth. At the reference site, the SMI was situated between 6.7 and 8.4 mbsf; it was located between 2.3 and 3.4 mbsf at the nonseep site and between 0.5 and 1.0 mbsf at the seep sites. Using the depth of the SMI as a first-order approximation for methane flux inferences (Bhatnagar et al., 2011; Luff & Wallmann, 2003), the reference site had the lowest upward fluxes. Data from the nonseep site indicate an intermediate methane flux. The highest fluxes can be assigned to the seep sites within the Lunde pockmark; here shallow gas hydrates were found, indicating that methane concentrations were sufficient to sustain gas hydrate precipitation.

Most negative δ^{13}C-DIC values (i.e., strongest depletions in ^{13}C) corresponded with depths of the SMI (−35.0‰ to −39.2‰ VPDB) at all sites. Below the SMI, DIC is gradually enriched in ^{13}C with depth; the most positive δ^{13}C-DIC value (30.7‰) was found in the SW seep at 10.4 mbsf in core GeoB21637-1 (Figure 3c).

4.3. Stable Carbon and Hydrogen Isotopic Signatures of Methane

Despite some gaps in sediment core recovery, high-resolution δ^{13}C-CH_4 versus depth profiles were obtained from void gas, headspace gas, and gas from pressure cores samples (Figure 4c). At the reference site, methane in the deepest sediments (between approximately 55 and 62.5 mbsf) was characterized by δ^{13}C-CH_4 values between about −65‰ and −59‰ VPDB. With decreasing depth, δ^{13}C-CH_4 values decreased with minimum δ^{13}C-CH_4 of approximately −95‰ found at approximately 10 mbsf, which was close to the depth of the SMI (approximately 8.4 mbsf).

At the nonseep site within the Lunde pockmark, δ^{13}C-CH_4 values between about −65‰ and −59‰ were between 22 and 8 mbsf, that is, shallower than at the reference site. Minimum δ^{13}C-CH_4 of approximately −76‰ were found at approximately 2.8 mbsf, which is about 0.5 m deeper than the SMI depth defined by the sulfate profiles. However, because gas samples that fell closer to the SMI and showed methane concentrations sufficient for δ^{13}C-CH_4 measurement were not available, maximum ^{13}C depletions of CH_4 at the nonseep site remain unclear. At the seep site in the SW sector of Lunde pockmark, methane was enriched in ^{13}C relative to the other two sites under investigation, with values generally ranging between −58‰ and −48‰. The most positive stable carbon isotope value of methane in headspace gas corresponds to that determined for methane bound in gas hydrates recovered from shallow sediment (−54‰ and −49‰; Figures 3c, 3d, and 4a).

Stable hydrogen isotope data are available for methane in headspace gas collected at the reference site and the nonseep site and in the deeper sediment from the SW seep, as well as for methane in shallow gas hydrates from both seep sites. Methane at depth showed δ^{2}H-CH_4 signatures of approx. −190‰ VSMOW at all sites (Figure 4b). Similar δ^{2}H-CH_4 values (−197‰ to −188‰) were measured for methane in shallow gas hydrates recovered from the seep sites (Table S7 in the supporting information).

4.4. Molecular Hydrocarbon Compositions

In contrast to the isotopic data presented above, where profiles can be generated throughout the entire core using headspace samples, the hydrocarbon molecular composition can only be obtained in sections where gas voids or gas hydrates were present. The deepest (~62 mbsf) gas sample for hydrocarbon molecular composition was obtained from the reference site and showed a relatively low hydrocarbon ratio (C_1/C_{2+}) of 253 (Figure 4c). C_1/C_{2+} gradually increased from 480 to 2,730 with decreasing depth between about 59 and 48 mbsf. In shallower (approximately 8 to 18 mbsf) sediment of the nonseep site, the C_1/C_{2+} ranged between ~1,900 and 2,900. Seep sites were sampled in the upper 13.4 mbsf. In these sediments, C_1/C_{2+} were <500 with only two exceptions: 1,840 at 4.2 mbsf and 1,000 at 13.4 mbsf.

4.5. Modeling Results

The reaction rates derived from our stable carbon isotopic mass balance calculation are illustrated in Figure 5b and listed in Table S8 in the supporting information. We derived rates for AOM, POCSR, and CP comparable to those of Hong et al. (2016), who applied transport-reaction modeling on a different set of gravity cores from the Lunde and Lomvi pockmarks. The similar model results provide confidence to our data interpretation. As DIC is involved in all the reactions considered, we compared the reaction rates with ΔF_{DIC} in Figure 5b. In general, AOM accounts for 83% to 99% of the overall sulfate reduction. In

terms of the source of methane, in situ microbial ME is responsible for 3% to 46% of the methane being consumed by AOM, with the largest percentage at the reference site and the smallest contribution at the seep sites. Within a broad depth zone that encompasses the SMI, between approximately 20% to 40% of the carbon is cycled between AOM and CO_2 reduction. As expected, AOM contributes more significantly to the DIC budget, with a 25% to 61% contribution to the DIC pool originating from organic matter degradation through both ME and sulfate reduction. The DIC contribution from organic matter seems to be smaller (25% to 34%) in the two seep locations compared to the other ones (48% to 61%). The observation of a smaller contribution from organic matter at the seep sites is supported by the lower dissolved ammonium content at these locations (Figure S7 in the supporting information). Hong et al. (2016) observed a similar variation between seep and nonseep sites in Vestnesa Ridge and interpreted this as resulting from the competition between methane and organic matter for sulfate reduction.

5. Discussion

5.1. Hydrocarbon Sources and Migration

In the Bernard diagram (Figure 4a), gas samples from the reference site where hydrates were absent reveal a mixture of thermogenic and microbial hydrocarbons, with clear evidence for an increase in the contribution of microbially sourced hydrocarbons with decreasing depth. All samples from sediment shallower than approximately 50 mbsf at the reference site clearly plot within the microbial hydrocarbon field, as do all samples from the nonseep site, which are shallower than 21.5 mbsf. This indicates de novo methane formation in shallow sediments even within the pockmark at sites located distant to emission sites. In contrast, the majority of gas samples, including hydrate-bound hydrocarbons from the seep sites (0.5–13.4 mbsf), plot within or close to the field assigned for thermogenic hydrocarbons, even though these cores sampled sediments shallower than 15.3 mbsf. A thermogenic origin for the deep methane is also inferred from the $\delta^{13}C$–$\delta^{2}H$-CH_4 relationships (Figure 4b).

The stable carbon and hydrogen isotope data investigated herein resemble those previously reported for hydrate-bound methane at the Lunde pockmark ($\delta^{13}C$-CH_4: −45.7‰ VPDB; $\delta^{2}H$-CH_4: −180‰ VSMOW; Fisher et al., 2011; Graves et al., 2017) and the nearby Lomvi pockmark ($\delta^{13}C$-CH_4: −51.6‰ to −47.7‰ VPDB; Panieri et al., 2017; Smith et al., 2014; for core positions see Figure S2 in the supporting information), and all point to a common hydrocarbon source beneath both pockmarks. To further explore whether the molecular composition of hydrocarbons in the recovered sediment reflect in situ production, we plot the molecular hydrocarbon data against its corresponding in situ sediment temperature, as calculated from geothermal gradients established during MSM57 (Figure 4d and Tables S4 and S5 in the supporting information). We compare our data with those reported for ODP Sites 909, 910, 912, and 986, drilled in the region comprising our study area (see Figure 1a for positions). The ODP data show the depth distribution with increasing temperature expected for a prevailing fraction of hydrocarbons originating from microbial in situ production and illustrate the contrast with sites sampled during the MSM57 expedition that contain a dominating fraction of hydrocarbons that migrated from a deeply seated thermogenic source. Vestnesa Ridge samples show a strong depletion in the C_1/C_{2+} ratios at equivalent formation temperatures. Hydrocarbons in the deeper samples recovered at the reference site have a significant component of migrated fluid. Moreover, the shallow samples from the seep sites undoubtedly reflect hydrocarbon migration from depth. The distribution shown in Figure 4d underlines the relevance of gas injections into shallow sediments at the crest of Vestnesa Ridge.

For the assessment of the formation depth range of thermogenic hydrocarbons below our study area, we use the geothermal gradients estimated using our heat flow data (Tables S4 and S5 in the supporting information) and assume that the measured gradients of 0.078 °C/m at reference sites and 0.081 °C/m within the Lunde pockmark follow a linear trend with depth. We further considered temperature ranges for thermocatalysis of organic matter, reportedly to begin at around 70 °C and to peak at approximately 150 °C (Hunt, 1996; Quigley & Mackenzie, 1988; Seewald, 2003), to arrive at a depth for thermogenic hydrocarbon generation in Vestnesa Ridge of >800 mbsf (Table 1). The assumption of a several hundred meters long migration of thermogenic hydrocarbons from our predicted source depth is consistent with seismic data that image faults and acoustic chimneys piercing through the approximately 195-m-thick GHSZ into deeper sediments (Plaza-Faverola et al., 2015). The source rock depth inferred from our study should be taken as rough estimate since

Table 1
Temperature Data Collected With the Head Flow Probe and MeBo MTLs at the Crest of Vestnesa Ridge (Bohrmann et al., 2017) and Resulting Formation Depths of Thermogenic Hydrocarbons (Hydrocarbon Formation Temperatures Adapted From Hunt (1996), Quigley and Mackenzie (1988), and Seewald (2003))

	Geothermal gradient (measured)	Formation depth of thermogenic hydrocarbons (calculated)	
	(°C/m)	(mbsf)	
		70 °C Start of thermogenesis	150 °C Maximum hydrocarbon production
Reference sites	0.078	897.4	1,923.1
Lunde pockmark	0.081	864.2	1,851.9

Note. Details of sediment temperature measurements are given in Text S2, Figure S1, and Tables S4 and S5 in the supporting information.

we extrapolated geothermal gradients based on data collected only to 55.4 mbsf; however, our inferences are in agreement with a Miocene source for the migrated hydrocarbons, as previously suggested based on petroleum system modeling (Dumke et al., 2016; Knies et al., 2018).

Collectively, the hydrocarbon data collected during MSM57 extends our knowledge of subseafloor hydrocarbon distribution at depth and allow us to better constrain focused gas migration along faults and chimneys, the presence of a more diffusively migrated thermogenic component at depth, and the relative contribution of microbially mediated methane as a function of site location. Furthermore, the molecular and stable C and H isotopic compositions of thermogenic hydrocarbons from deep core sections at the reference site approximate those of hydrocarbons bound in shallow gas hydrates recovered from the seep sites. Therefore, hydrocarbons forming the gas hydrates reflect the deeply buried hydrocarbon source. MeBo drilling into a chimney structure with well-imaged discontinuities and amplitude anomalies in the upper tens of meters below seafloor (Figure 1g) clearly establishes a structural control for thermogenic gas migration along this high permeability pathway, resembling a fracture and fault network. This channeled flow path connects hydrocarbons likely generated at depths >800 mbsf to the shallow sediments at flow rates high enough to sustain the gas plumes observed above the seafloor (Bünz et al., 2012; Hustoft et al., 2009; Panieri et al., 2017; Smith et al., 2014). This methane flux sustains microbial activity (Yao et al., 2019) and gas hydrate formation within the Lunde pockmark. Whereas the chimney structure sampled with MeBo provides a clear conduit for rapid gas migration, our data from the reference site also highlights the fact that, in addition to fault-controlled migration, there is also a distributed upward transport of thermogenic hydrocarbons in this region, as observed in the thermogenic migrated fingerprint as shallow as 60 mbsf at the reference site. These hydrocarbons might have migrated into shallow strata along some of the many faults occurring along the Vestnesa Ridge (Figure 1d; Figure 2 in Plaza-Faverola et al., 2015).

5.2. Distribution of Shallow Gas Hydrates

Our study area lies well within the GHSZ (e.g., Vogt et al., 1994) and a widespread BSR indicates the presence of gas hydrates in a zone reaching down to about 195 mbsf (Bünz et al., 2012; Plaza-Faverola et al., 2017). Gas hydrates recovered from the uppermost 6 m of deposits in the Lunde pockmark (Fisher et al., 2011) and the adjacent Lomvi pockmark (Panieri et al., 2017; Smith et al., 2014) document gas hydrate formation in shallow sediments, in locations of active gas migration evidenced as acoustic chimneys in the seismic data (Bünz et al., 2012; Plaza-Faverola et al., 2015).

In this study we establish the shallow gas hydrate distribution via IR imaging (Sultan et al., 2014; Wei et al., 2015; Weinberger et al., 2005) of all sediment cores recovered during expedition MSM57. Our comprehensive data set demonstrates that gas hydrates are present only at the seep sites (Figure 2), that is, at the locations fed by gas migration along deeply rooted faults and chimney structures (Figures 1d, 1f, and 1g). We established the shallowest limit of the gas hydrate occurrence zone to be at ~0.6 mbsf (GeoB21609-2, SW sector of Lunde pockmark) and at 2.3 mbsf (GeoB21612-1, SE sector). It is likely that at the seep site in the southwest the shallow gas hydrate-bearing zone was entirely penetrated, given the absence of gas hydrates in deeper sections of cores GeoB21616-1 (greater than approximately 1 mbsf), GeoB21621-1 (greater than

approximately 6 mbsf), and GeoB21637-1 (greater than approximately 11 mbsf), suggesting that the presence of these shallow gas hydrates is limited to top sediments fed by a fracture network inside the chimney. If the distance between the SMI and the top of gas hydrate occurrence are taken as indicative of relative methane flux intensity (Bhatnagar et al., 2011; Luff & Wallmann, 2003), then SE seep (distance <2.5 m) apparently experiences a higher fluid flux, relative to that in the SW (distance ~ 5.4 m). This difference may be attributed to spatial and/or temporal fluid dynamics at these sites. Regardless of this difference, our results show that the shallow gas hydrate zone associated with gas seepage reaches 8 mbsf and spreads over more than 10 m in distance. The molecular and isotopic similarities between shallow hydrate-bound methane and that of methane in deeper sediments show that hydrate-bound hydrocarbons are largely unaffected by early diagenetic modifications and are appropriate to evaluate properties of hydrocarbons rising from greater depth.

The abundance of nonmethane hydrocarbons in the hydrate-fueling gas suggests incipient formation of gas hydrate crystal structure sII (Sloan, 2003). The close spatial relation between gas hydrate occurrences and the emission of hydrocarbons in the free gas phase at the seep sites indicates that hydrate formation at these sites is sustained by gas rather than aqueous transport of hydrocarbons (e.g., Bohrmann et al., 1998; Sultan et al., 2014; Torres et al., 2004). In addition, our data support the suggestion that gas hydrate bubble coating may enable ascending bubbles in the water column to survive at least to the top of gas stability boundary for sII hydrates, at approximately 340 mbsl, consistent with observations in hydroacoustic flare mapping (Smith et al., 2014).

The absence of gas hydrates in the sampled sediments at the reference site and the nonseep site within Lunde pockmark can be attributed to methane concentrations below solubility. The methane flux system in this area appears to be primarily controlled by focused flow along faults and specific fracture networks within chimneys (Bünz et al., 2012; Panieri et al., 2017; Plaza-Faverola et al., 2015) that both bypass these two nonseep sites (Figures 1d–1g). Methane at these sites is in the most part the result of in situ microbial processes (see carbon cycling section 5.3), as diffuse migration of thermogenic sources appears to be limited to depths >~50 mbsf.

5.3. Carbon Cycling Pathways

In the previous sections we discussed the role of molecular and isotopic strategies to infer carbon supply to shallow sediments from depth. Here we focus on carbon cycling pathways in the shallow sediments of the Lunde pockmark by investigating the methane, DIC, and organic carbon in terms of their carbon isotopic fingerprints (Figures 3 and 5).

TOC contents in MeBo cores were on average 0.8% at the reference site (0–59.2 mbsf) and at the nonseep site (0–7.5 mbsf), while at the seep sites (0–15.1 mbsf) TOC contents were 0.9–1.0% (Table S6 in the supporting information). TOC contents exceeding 2.0% have also been reported for shallow sediments recovered from our study area (Åström et al., 2018; Sztybor & Rasmussen, 2017b). Negative excursions in $\delta^{13}C\text{-}C_{org}$ in shallow sediments point to a contribution of methane-based de novo biosynthesis of organic matter (Figure S5 in the supporting information). Strongest deviations in the stable carbon isotopic composition of organic carbon towards more negative values ($\Delta\delta^{13}C\text{-}C_{org}$ approximately 2.7‰ from average) are observed in sediments within the pockmark and in particular at the seep sites. It is likely that intense supply of deep-sourced methane fuels microbial mats and other chemoauthotrophic activity at these sites (Yao et al., 2019), that is, methane-derived carbon is incorporated into biomass produced in situ. Constant methane availability has been postulated as the cause for considerably higher infaunal diversity and biomass observed within the Lunde and Lomvi pockmarks relative to that at background stations (Åström et al., 2018; Panieri et al., 2015).

The organic matter concentration in this region (TOC: 0.2–1.5%; Figure S4 and Table S6 in the supporting information), whether due to photoautotrophy or chemoautotrophy, is sufficient to support microbial hydrocarbon production in uppermost 60 mbsf in this region. The drastic increase in C_1/C_{2+} ratios and ^{13}C depletions in methane with decreasing depth observed at the reference site between about 59 and 49 mbsf (Figures 3a, 4a, and 4c), reflects substantial in situ methane production, consistent with microbial methane formation in shallow pockmark sediments inferred for gas samples collected from the top 1.75 m of sediments in the adjacent Lomvi pockmark (Panieri et al., 2017). These inferences are supported by stable carbon isotope mass balance calculations (Figure 5). In the deepest samples from the reference site (i.e.,

those representing the isotopic composition of carbon species arriving at the SMI) the δ^{13}C-CH_4 is −59.2‰, whereas the δ^{13}C-DIC is 12.1‰ (Figure 3a and Table S3 in the supporting information). If the isotope fractionation factor ($\varepsilon_C \approx \delta^{13}$C-DIC − δ^{13}C-CH_4 = 71.3‰) reflects equal contributions of CO_2 and CH_4 to the overall isotopic disproportionation during organic matter-based ME that would correspond to an isotopic signature of the parent TOC of approximately −23.6‰, which is similar to the measured $\delta^{13}C\text{-}C_{org}$ (Figure S5 in the supporting information). A similar approach for the nonseep site, also indicates a component of the methane being generated by in situ ME. However, that is not the case for both seep sites, for which a similar mass balance approach yields a value for $\delta^{13}C\text{-}C_{org}$ of approximately −13‰. This value is far too heavy from the measured isotopic composition of organic carbon, that is, consistent with our inferences that methane at seep sites migrated from depth and that the methane transport in the gas phase is decoupled from the inorganic carbon pool, which is mostly present in the dissolved phase.

Microbial methane production in typical marine sediment is believed to be most effective at temperatures less than approximately 30 °C (Hunt, 1996; Valentine, 2011), which in the area around Lunde pockmark occurs in sediments shallower than approximately 375 mbsf considering a linear trend of the measured geothermal gradient. An increase in ammonium concentrations downcore (Figure S7 in the supporting information) indicates that microbial methane production below the SMI occurs from the SMI to 60 mbsf and that significant methane production by psychrophilic methanogens occurs in the temperature range between approximately −0.1 °C and +3.9 °C (8.4 to 60 mbsf). Psychrophilic methanogen activity in permafrost soils and marine sediments at negative temperatures, similar to the inferred conditions at our site, has previously been reported (e.g., Rivkina et al., 2004; Whiticar et al., 1986). The increase in δ^{13}C-DIC values below the SMI and the isotope fractionation factor ε_C reaching values of ˜73‰ at depth (Figure 3) are consistent with the typical microbial discrimination against ^{13}C during carbonate reduction (Paull et al., 2000; Whiticar, 1999). Collectively, all these data support a significant contribution of microbial methane to the overall carbon cycle regime within the Vestnesa Ridge sediment.

Our model results show that AOM, rather than organic matter degradation, dominates the sulfate consumption at all sites (Figure 5b and Table S8 in the supporting information). Consequently, a comparably higher fraction of TOC is able to escape from sulfate reduction, gets buried into the zone below the SMI, and sustains ME there, which is reflected in the isotope mass balance of the reference site. This result also supports our inferences on the estimates of methane flux rates based on the depth of the SMI in section 4.2. AOM at all sites consumes almost all dissolved methane, either thermogenic or microbially generated, and leads to generation of a DIC pool that is significantly depleted in ^{13}C (up to –39‰) relative to seawater DIC (Figure 3; e.g., Heuer et al., 2009; Malinverno & Pohlman, 2011). Whereas this microbial methane filter and the associated generation of isotopically light DIC has been known for decades (e.g., Borowski, 2004; Claypool & Threlkeld, 1983; Hoehler et al., 2000), more recent evidence indicates a concomitant depletion in ^{13}C of the methane present at the SMI (e.g., Chuang et al., 2019; Hong et al., 2014; Pohlman et al., 2008). Well-defined ^{13}C depletions in both methane and inorganic carbon are apparent in our data for the reference site and the nonseep site (Figures 3a and 3b). Such unexpected coupled depletions in the light carbon isotope at the SMI have been previously explained by carbon cycling between AOM and ME in a narrow zone centered at the SMI, where fractionated, ^{13}C-depleted CO_2 is used for microbial de novo (or secondary) methane production through carbonate reduction in the uppermost methanogenic zone (Borowski, 2004; Borowski et al., 1997; Chen et al., 2010; Haese et al., 2003; Hong et al., 2014; Paull et al., 2000; Pohlman et al., 2008; Ussler & Paull, 2008). Results from our box model approach agree with this previously postulated mechanism, that is, the isotopic mass balance requires that a significant component of the methane currently present at the SMI must originate from reduction of light carbon generated as DIC by AOM in the uppermost methanogenic zone (CR in Figure 5 and Table S3 in the supporting information).

Model calculations also show that depletions in ^{13}C of the DIC measured at SMI depths of seep and nonseep sites (Figures 3a–3d and Table S3 in the supporting information) are indicative of intense AOM activity at all sites. AOM rates, however, are higher at seep sites where estimated rates yield values of 41.7 $\mu mol \times cm^{-2} \times year^{-1}$ (seep site SW) and 32.5 $\mu mol \times cm^{-2} \times year^{-1}$ (seep site SE), respectively. Similarly, elevated AOM rates were previously estimated at other seep locations in Lunde and Lomvi pockmark (Hong et al., 2016; Panieri et al., 2017). In contrast, AOM rates at our reference site are an order of magnitude lower than those at seep sites (Figure 5b and Table S8 in

the supporting information). Such inferences would not be apparent by considering solely the methane stable carbon isotopic composition, which at the seep sites show no measurable depletion at the SMI (Figures 3c and 3d).

The current SMI in cores from both seep sites is deeper than 0.5 mbsf (Figure 3). Rates of carbonate precipitation from both seep sites, as calculated from the pore water calcium and magnesium profiles (see Data Set S1), are 2 to 10 times higher than the rates from the nonseep and reference sites, respectively (Figure 5b). Nonetheless, compared to past carbonate crust-forming episodes as reported by Himmler et al. (2019) for the SW seep, the current precipitation rates at both of the seep sites studied herein are likely to be lower than in the past, probably because of lower methane fluxes and oxidation rates. Given that carbonate nodules have not been found in sediment intervals at the SMI, we suggest that establishment of the SMI at present depths has happened relatively recently and that the extent of carbonate precipitation is rather limited, without formation of macroscopic carbonate nodules so far.

Previous observations that microbial communities require a supply of methane in the dissolved form (Knittel & Boetius, 2009; Sommer et al., 2006) led to the commonly accepted assumption that at sites of active gas discharge, methane bypasses the microbial filter with little consumption by AOM. Our combined data/model approach, however, clearly indicates that AOM is very active at the seep sites, where methane gas is known to escape and feed the observed plumes in the water column (Bünz et al., 2012; Hustoft et al., 2009; Panieri et al., 2017; Smith et al., 2014). This apparent paradigm, that is, microbial methane consumption at sites where most of the methane is supplied in the gas phase, points to the active transfer of methane from gas to the dissolved phase at the SMI, as documented by Mogollón et al. (2009) for the Eckernförde system. Not only are the AOM rates highest at seep sites, but the secondary ME rates (CR) are also highest at sites of rapid discharge of methane gas (Figure 5b and Table S8 in the supporting information), reflecting a very fast carbon metabolic cycle at the SMI of active methane seep sites. These conclusions are not apparent in changes in the stable carbon isotopic composition of methane ($\delta^{13}C\text{-}CH_4$) simply because the high methane flux from depth masks any changes in the measured carbon isotopic composition of the overall methane pool.

6. Conclusions

Investigations at the Vestnesa Ridge over the past decade have established the presence of a high density of pockmarks and persistent gas emissions at the seafloor. Gas hydrates have been sampled from shallow depth and a regional BSR substantiates the presence of gas hydrates and free gas at depth. Characterization of the hydrocarbon system thus far has been limited to analyses of emanating gas, near surface gas hydrates, and short cores from the uppermost approximately 6 m of sediment.

Sediment cores collected with the deep-sea drill rig MARUM-MeBo70 during the expedition MSM57 in 2016, sampled the deeper sediment section (up to 62.5 mbsf) from the Lunde pockmark region on the crest of Vestnesa Ridge, and allowed us to better understand the hydrocarbon sources, migration pathways, and carbon cycling processes at this location.

$\delta^{13}C$-DIC, methane, and sulfate depth profiles indicate that the study sites are characterized by different rates of fluid flux, with lowest fluxes at our reference station, intermediate at a nonseep site within the pockmark and highest at two sites drilled at sites of active seepage. At the reference site, the deepest gas sample (62 mbsf) has a major component of migrated thermogenic hydrocarbons, as evidenced by the methane to higher hydrocarbon ratio in the gas phase (C_1/C_{2+} ~ 250) relative to formation temperatures and further demonstrated by carbon and hydrogen isotope data. With decreasing depth, the fraction of microbial methane increases, with a prevalence of microbial hydrocarbons in sediments shallower than approximately 50 mbsf. Microbial methane production also dominates the hydrocarbon component at the nonseep site within the pockmark. Isotope mass balances of carbon among the TOC, DIC, and CH_4 pools are consistent with these inferences. Collectively, our data/model from the reference site and the seep site reveal active in situ methane generation at sediment temperatures <4 °C.

Despite abundant organic matter in the shallow sediments (mean TOC 0.8%), microbial formation at nonseep sites does not produce sufficient methane for gas hydrate precipitation. The hydrocarbons that sustain shallow gas hydrates at sites of active seepage are transported in the gas phase through faults and fracture

networks in chimneys imaged in the seismic record. Stable C and H isotopic compositions (−54.1‰ to −48.7‰ VPDB; −197‰ to −188‰ VSMOW) in concert with C_1/C_{2+} ratios <425 suggest a thermogenic origin for the methane bound in shallow hydrates. The gas migrates from depths >800 mbsf, as estimated using the thermal gradient derived from temperature data collected down to 55 mbsf. These hydrocarbons possibly originate from deeply buried Miocene source rocks and are focused upward through a deep-rooted fault system. Gas hydrates predominantly precipitate from these thermogenic hydrocarbons and the hydrate-bound hydrocarbons are representative for the gas chemical properties of the deeply buried source.

Depletions in ^{13}C of the DIC at the SMI are documented at all sites, with a $\delta^{13}C$-DIC of -37 ± 2‰ VPDB, independent of site-specific fluid flux magnitude and transport mechanisms. Depletions in ^{13}C of the methane at the SMI are indicative of conversion of a fraction of the DIC generated by AOM back to methane, via secondary carbonate reduction (CR). Box model results show that sites characterized by a high flux of gaseous methane from deeper sources support highest rates of methane consumption (by AOM) and of methane generation (by CR). At low-flux sites the microbial filter removes all of the available methane, whereas at high-flux sites only a small fraction of methane is consumed by microbes such that the carbon isotopic composition measured in the bulk methane pool is not altered from the values at the source, thus the roles of AOM and CR processes at the SMI are not observable in the isotopic composition of the total methane pool. Whereas the majority of methane bypasses the microbial filter rapidly at the high-flux sites and escapes into the water column, the isotopic change in DIC measured at both seep sites shows that a fraction of the advecting gas is dissolved in the pore water and made available to microbes, which consume it at rates of 33 to 42 $\mu mol \times cm^{-2} \times year^{-1}$.

Data Availability Statement

Relevant data are made available through the World Data Center PANGAEA® (www.pangaea.de; Pape et al., 2019). Additional information is available to interested readers on request.

Acknowledgments
We would like to acknowledge the master and crew of R/V MARIA S. MERIAN for their friendly assistance during cruise MSM57. The excellent support by Dr. T. Freudenthal and the team of the seafloor drill rig "MeBo70" (MARUM) is gratefully acknowledged. D. Wunsch (Corsyde International, Berlin) is thanked for preparing and maintaining the pressure core barrels for MeBo (MDP). We are grateful to J. Malnati (Department of Geosciences, University of Bremen) for sample preparation and analyses as well as D. Dasbach and Dr. D. Monien (ZMT, Bremen) for conducting $\delta^{13}C$-C_{org} measurements. Dr. E. Schefuss (MARUM) is thanked for his support during stable isotope analysis of methane. The constructive comments by two anonymous reviewers and the associate editor, Dr. I. Pecher, greatly helped to improve an earlier version of the manuscript. This study was financed by the German Research Foundation (DFG) as well as by funds from the Research Council of Norway through its Centres of Excellence funding scheme, project 223259 and Statoil ASA. M. E. T. acknowledges support from the U.S. Department of Energy (DE-FE0013531) and the Hanse-Wissenschaftskolleg (HWK), Germany. W. -L. H and A. L. acknowledge support from the NORCRUST project funded by the Norwegian Research Council (project 255150).

References

Aloisi, G., Bouloubassi, I., Heijs, S. K., Pancost, R. D., Pierre, C., Sinninghe Damsté, J. S., et al. (2002). CH_4-consuming microorganisms and the formation of carbonate crusts at cold seeps. *Earth and Planetary Science Letters*, *203*(1), 195–203. https://doi.org/10.1016/S0012-821X(02)00878-6

Ambrose Jr., W. G., Panieri, G., Schneider, A., Plaza-Faverola, A., Carroll, M. L., Åström, E. K. L., et al. (2015). Bivalve shell horizons in seafloor pockmarks of the last glacial-interglacial transition: A thousand years of methane emissions in the Arctic Ocean. *Geochemistry, Geophysics, Geosystems*, *16*, 4108–4129. https://doi.org/10.1002/2015gc005980

Åström, E. K. L., Carroll, M. L., Ambrose Jr., W. G., Sen, A., Silyakova, A., & Carroll, J. (2018). Methane cold seeps as biological oases in the high-Arctic deep sea. *Limnology and Oceanography*, *63*(S1), S209–S231. https://doi.org/10.1002/lno.10732

Bernard, B., J. M. Brooks, and W. M. Sackett (1977), A geochemical model for characterization of hydrocarbon gas sources in marine sediments, paper presented at Offshore Technology Conference, Offshore Technology Conference, Houston, Texas, 02.-05.05.1977.

Bhatnagar, G., Chatterjee, S., Chapman, W. G., Dugan, B., Dickens, G. R., & Hirasaki, G. J. (2011). Analytical theory relating the depth of the sulfate-methane transition to gas hydrate distribution and saturation. *Geochemistry, Geophysics, Geosystems*, *12*, Q03003. https://doi.org/10.1029/2010gc003397

Boetius, A., Ravenschlag, K., Schubert, C. J., Rickert, D., Widdel, F., Gieseke, A., et al. (2000). A marine microbial consortium apparently mediating anaerobic oxidation of methane. *Nature*, *407*(6804), 623–626. https://doi.org/10.1038/35036572

Boetius, A., & Wenzhöfer, F. (2013). Seafloor oxygen consumption fuelled by methane from cold seeps. *Nature Geoscience*, *6*(9), 725–734. https://doi.org/10.1038/ngeo1926

Bohrmann, G., Ahrlich, F., Bergenthal, M., Bünz, S., Düßmann, R., dos Santos Ferreira, C., et al. (2017). R/V MARIA S. MERIAN Cruise Report MSM57, Gas Hydrate Dynamics at the Continental Margin of Svalbard, Reykjavik – Longyearbyen – Reykjavik, 29 July – 07 September 2016., *Berichte, MARUM - Zentrum für Marine Umweltwissenschaften, Fachbereich Geowissenschaften, Universität Bremen*: Bremen, 204. Retrieved from http://nbn-resolving.de/urn:nbn:de:gbv:46-00105895-15

Bohrmann, G., Greinert, J., Suess, E., & Torres, M. (1998). Authigenic carbonates from the Cascadia subduction zone and their relation to gas hydrate stability. *Geology*, *26*(7), 647–650. https://doi.org/10.1130/0091-7613(1998)026<0647:ACFTCS>2.3.CO;2

Borowski, W. S. (2004). A review of methane and gas hydrates in the dynamic, stratified system of the Blake Ridge region, offshore southeastern North America. *Chemical Geology*, *205*(3–4), 311–346. https://doi.org/10.1016/j.chemgeo.2003.12.022

Borowski, W. S., Paull, C. K., & Ussler, W. III (1997). Carbon cycling within the upper methanogenic zone of continental rise sediments: An example from the methane-rich sediments overlying the Blake Ridge gas hydrate deposits. *Marine Chemistry*, *57*(3-4), 299–311. https://doi.org/10.1016/S0304-4203(97)00019-4

Bünz, S. (2013), R/V Helmer Hanssen Cruise No. 2013007 - Part I, University of Tromsø cruise report, Tromsø – Longyearbyen, 08-07-13 to 21-07-13: Tromsø (Institutt for Geologi, Univ. i Tromsø), 33. https://doi.org/10.3289/CR_ECO2_24445.

Bünz, S., Polyanov, S., Vadakkepuliyambatta, S., Consolaro, C., & Mienert, J. (2012). Active gas venting through hydrate-bearing sediments on the Vestnesa Ridge, offshore W-Svalbard. *Marine Geology*, *332–334*, 189–197. https://doi.org/10.1016/j.margeo.2012.09.012

Chen, N. C., Yang, T. F., Hong, W.-L., Chen, H.-W., Chen, H.-C., Hu, C.-Y., et al. (2017). Production, consumption, and migration of methane in accretionary prism of southwestern Taiwan. *Geochemistry, Geophysics, Geosystems*, *18*, 2970–2989. https://doi.org/10.1002/2017GC006798

Chen, Y., Ussler, W. III, Haflidason, H., Lepland, A., Rise, L., Hovland, M., & Hjelstuen, B. O. (2010). Sources of methane inferred from pore-water $\delta^{13}C$ of dissolved inorganic carbon in Pockmark G11, offshore Mid-Norway. *Chemical Geology*, *275*(3-4), 127–138. https://doi.org/10.1016/S0304-4203(97)00019-4

Chuang, P.-C., Yang, T. F., Wallmann, K., Matsumoto, R., Hu, C.-Y., Chen, H.-W., et al. (2019). Carbon isotope exchange during anaerobic oxidation of methane (AOM) in sediments of the northeastern South China Sea. *Geochimica et Cosmochimica Acta*, *246*, 138–155. https://doi.org/10.1016/j.gca.2018.11.003

Claypool, G. E., and C. N. Threlkeld (1983), Anoxic diagenesis and methane generation in sediments of the Blake Outer Ridge, Deep Sea Drilling Project Site 533, Leg 76, *Proc. DSDP, Init. Repts., 76*: Washington, D.C. (Deep Sea Drilling Project), 391-402. https://doi.org/10.2973/dsdp.proc.76.109.1983

Clayton, C. (1991). Carbon isotope fractionation during natural gas generation from kerogen. *Marine and Petroleum Geology*, *8*(2), 232–240. https://doi.org/10.1016/0264-8172(91)90010-X

Crane, K., Sundvor, E., Buck, R., & Martinez, F. (1991). Rifting in the northern Norwegian-Greenland Sea: Thermal tests of asymmetric spreading. *Journal of Geophysical Research*, *96*(B9), 14,529–14,550. https://doi.org/10.1029/91JB01231

Crémière, A., Strauss, H., Sebilo, M., Hong, W.-L., Gros, O., Schmidt, S., et al. (2017). Sulfur diagenesis under rapid accumulation of organic-rich sediments in a marine mangrove from Guadeloupe (French West Indies). *Chemical Geology*, *454*, 67–79. https://doi.org/10.1016/j.chemgeo.2017.02.017

Dickens, G. R., D. Schroeder, K.-U. Hinrichs, and The Leg 201 Shipboard Scientific Party (2003), The pressure core sampler (PCS) on ODP Leg 201: General operations and gas release, *Proc. ODP, Init. Repts., 201*: College Station, TX (Ocean Drilling Program). https://doi.org/10.2973/odp.proc.ir.201.103.2003

Dumke, I., Burwicz, E. B., Berndt, C., Klaeschen, D., Feseker, T., Geissler, W. H., & Sarkar, S. (2016). Gas hydrate distribution and hydrocarbon maturation north of the Knipovich Ridge, western Svalbard margin. *Journal of Geophysical Research: Solid Earth*, *121*, 1405–1424. https://doi.org/10.1002/2015JB012083

Eiken, O., & Hinz, K. (1993). Contourites in the Fram Strait. *Sedimentary Geology*, *82*(1), 15–32. https://doi.org/10.1016/0037-0738(93)90110-Q

Engen, Ø., Faleide, J. I., & Dyreng, T. K. (2008). Opening of the Fram Strait gateway: A review of plate tectonic constraints. *Tectonophysics*, *450*(1), 51–69. https://doi.org/10.1016/j.tecto.2008.01.002

Fisher, R. E., Sriskantharajah, S., Lowry, D., Lanoisellé, M., Fowler, C. M. R., James, R. H., et al. (2011). Arctic methane sources: Isotopic evidence for atmospheric inputs. *Geophysical Research Letters*, *38*, L21803. https://doi.org/10.1029/2011gl049319

Freudenthal, T., & Wefer, G. (2013). Drilling cores on the sea floor with the remote-controlled sea floor drilling rig MeBo. *Geoscientific Instrumentation, Methods and Data Systems*, *2*, 329–337. https://doi.org/10.5194/gi-2-329-2013

Graves, C. A., James, R. H., Sapart, C. J., Stott, A. W., Wright, I. C., Berndt, C., et al. (2017). Methane in shallow subsurface sediments at the landward limit of the gas hydrate stability zone offshore western Svalbard. *Geochimica et Cosmochimica Acta*, *198*, 419–438. https://doi.org/10.1016/j.gca.2016.11.015

Haese, R. R., Meile, C., Van Cappellen, P., & De Lange, G. J. (2003). Carbon geochemistry of cold seeps: Methane fluxes and transformation in sediments from Kazan mud volcano, eastern Mediterranean Sea. *Earth and Planetary Science Letters*, *212*, 361–375. https://doi.org/10.1016/S0012-821X(03)00226-7

Heuer, V. B., Pohlman, J. W., Torres, M. E., Elvert, M., & Hinrichs, K.-U. (2009). The stable carbon isotope biogeochemistry of acetate and other dissolved carbon species in deep subseafloor sediments at the northern Cascadia Margin. *Geochimica et Cosmochimica Acta*, *73*(11), 3323–3336. https://doi.org/10.1016/j.gca.2009.03.001

Himmler, T., Sahy, D., Martma, T., Bohrmann, G., Plaza-Faverola, A., Bünz, S., et al. (2019). A 160,000-year-old history of tectonically controlled methane seepage in the Arctic. *Science Advances*, *5*(9), eaaw1450. https://doi.org/10.1126/sciadv.aaw1450

Hoehler, T. M., W. S. Borowski, M. J. Alperin, N. M. Rodriguez, and C. R. Paull (2000), Model, stable isotope, and radiotracer characterization of anaerobic methane oxidation in gas hydrate-bearing sediments of the Blake Ridge, *Proc. ODP, Sci. Res., 164*: College Station, TX (Ocean Drilling Programm), 79-85. https://doi.org/10.2973/odp.proc.sr.164.242.2000

Hong, W.-L., Sauer, S., Panieri, G., Ambrose Jr., W. G., James, R. H., Plaza-Faverola, A., & Schneider, A. (2016). Removal of methane through hydrological, microbial, and geochemical processes in the shallow sediments of pockmarks along eastern Vestnesa Ridge (Svalbard). *Limnology and Oceanography*, *61*, S324–S343. https://doi.org/10.1002/lno.10299

Hong, W.-L., Torres, M. E., Kim, J.-H., Choi, J., & Bahk, J.-J. (2013). Carbon cycling within the sulfate-methane-transition-zone in marine sediments from the Ulleung Basin. *Biogeochemistry*, *115*(1-3), 129–148. https://doi.org/10.1007/s10533-012-9824-y

Hong, W.-L., Torres, M. E., Kim, J.-H., Choi, J., & Bahk, J.-J. (2014). Towards quantifying the reaction network around the sulfate–methane-transition-zone in the Ulleung Basin, East Sea, with a kinetic modeling approach. *Geochimica et Cosmochimica Acta*, *140*, 127–141. https://doi.org/10.1016/j.gca.2014.05.032

Howe, J. A., Shimmield, T. M., Harland, R. E. X., & Eyles, N. (2008). Late Quaternary contourites and glaciomarine sedimentation in the Fram Strait. *Sedimentology*, *55*(1), 179–200. https://doi.org/10.1111/j.1365-3091.2007.00897.x

Hunt, J. M. (1996). *Petroleum geochemistry and geology*, (2nd ed., pp. 743). W.H. Freeman.

Hustoft, S., Bünz, S., Mienert, J., & Chand, S. (2009). Gas hydrate reservoir and active methane-venting province in sediments on < 20 Ma young oceanic crust in the Fram Strait, offshore NW-Svalbard. *Earth and Planetary Science Letters*, *284*(1-2), 12–24. https://doi.org/10.1016/j.epsl.2009.03.038

Knies, J., Daszinnies, M., Plaza-Faverola, A., Chand, S., Sylta, Ø., Bünz, S., et al. (2018). Modelling persistent methane seepage offshore western Svalbard since early Pleistocene. *Marine and Petroleum Geology*, *91*, 800–811. https://doi.org/10.1016/j.marpetgeo.2018.01.020

Knies, J., Matthiessen, J., Vogt, C., Laberg, J. S., Hjelstuen, B. O., Smelror, M., et al. (2009). The Plio-Pleistocene glaciation of the Barents Sea–Svalbard region: A new model based on revised chronostratigraphy. *Quaternary Science Reviews*, *28*(9), 812–829. https://doi.org/10.1016/j.quascirev.2008.12.002

Knies, J., Mattingsdal, R., Fabian, K., Grøsfjeld, K., Baranwal, S., Husum, K., et al. (2014). Effect of early Pliocene uplift on late Pliocene cooling in the Arctic–Atlantic gateway. *Earth and Planetary Science Letters*, *387*, 132–144. https://doi.org/10.1016/j.epsl.2013.11.007

Knittel, K., & Boetius, A. (2009). Anaerobic oxidation of methane: Progress with an unknown process. *Annual Review of Microbiology*, *63*(1), 311–334. https://doi.org/10.1146/annurev.micro.61.080706.093130

Kvenvolden, K. A., and T. J. McDonald (1986), Organic geochemistry on the Joides Resolution: An assay, Technical Note: Texas A&M Univ, College Station, Tex. (Ocean Drilliing Program), *147*.

Luff, R., & Wallmann, K. (2003). Fluid flow, methane fluxes, carbonate precipitation and biogeochemical turnover in gas hydrate-bearing sediments at Hydrate Ridge, Cascadia Margin: Numerical modeling and mass balances. *Geochimica et Cosmochimica Acta*, *67*(18), 3403–3421. https://doi.org/10.1016/S0016-7037(03)00127-3

Malinverno, A., & Pohlman, J. W. (2011). Modeling sulfate reduction in methane hydrate-bearing continental margin sediments: Does a sulfate-methane transition require anaerobic oxidation of methane? *Geochemistry, Geophysics, Geosystems*, *12*, Q07006. https://doi.org/10.1029/2011gc003501

Mattingsdal, R., Knies, J., Andreassen, K., Fabian, K., Husum, K., Grøsfjeld, K., & De Schepper, S. (2014). A new 6 Myr stratigraphic framework for the Atlantic–Arctic Gateway. *Quaternary Science Reviews*, *92*, 170–178. https://doi.org/10.1016/j.quascirev.2013.08.022

Mogollón, J. M., L'Heureux, I., Dale, A. W., & Regnier, P. (2009). Methane gas-phase dynamics in marine sediments: A model study. *American Journal of Science*, *309*(3), 189–220. https://doi.org/10.2475/03.2009.01

Panieri, G., Bünz, S., Fornari, D. J., Escartin, J., Serov, P., Jansson, P., et al. (2017). An integrated view of the methane system in the pockmarks at Vestnesa Ridge, 79°N. *Marine Geology*, *390*, 282–300. https://doi.org/10.1016/j.margeo.2017.06.006

Panieri, G., Fornari, D. J., Serov, P., Åstrom, E. K. L., Plaza-Faverola, A., Mienert, J., Torres, M., et al. (2015). Gas hydrate, carbonate crusts, and chemosynthetic organisms on a Vestnesa Ridge pockmark - preliminary findings. *Fire in the Ice*, *15*(2), 14–17.

Panieri, G., James, R. H., Camerlenghi, A., Westbrook, G. K., Consolaro, C., Cacho, I., et al. (2014). Record of methane emissions from the West Svalbard continental margin during the last 23.500 yrs revealed by $\delta^{13}C$ of benthic foraminifera. *Global and Planetary Change*, *122*, 151–160. https://doi.org/10.1016/j.gloplacha.2014.08.014

Pape, T., Bahr, A., Rethemeyer, J., Kessler, J. D., Sahling, H., Hinrichs, K. U., et al. (2010). Molecular and isotopic partitioning of low-molecular weight hydrocarbons during migration and gas hydrate precipitation in deposits of a high-flux seepage site. *Chemical Geology*, *269*(3-4), 350–363. https://doi.org/10.1016/j.chemgeo.2009.10.009

Pape, T., Geprägs, P., Hammerschmidt, S., Wintersteller, P., Wei, J., Fleischmann, T., et al. (2014). Hydrocarbon seepage and its sources at mud volcanoes of the Kumano forearc basin, Nankai Trough subduction zone. *Geochemistry, Geophysics, Geosystems*, *15*, 2180–2194. https://doi.org/10.1002/2013gc005057

Pape, T., Hohnberg, H. J., Wunsch, D., Anders, E., Freudenthal, T., Huhn, K., & Bohrmann, G. (2017). Design and deployment of autoclave pressure vessels for the portable deep-sea drill rig MeBo (Meeresboden-Bohrgerät). *Scientific Drilling*, *23*, 29–37. https://doi.org/10.5194/sd-23-29-2017

Pape, T., J. Malnati, and G. Bohrmann (2019): Physical properties, gas composition, and $\delta^{13}C$-DIC measured on sediment cores from an active pockmark on Vestnesa Ridge, Arctic Ocean. PANGAEA, https://doi.org/10.1594/PANGAEA.905864

Paull, C. K., T. D. Lorenson, W. S. Borowski, W. Usler III, Olsen K., and N. M. Rodriguez (2000), Isotopic composition of CH_4, CO_2 species, and sedimentary organic matter within samples from the Blake Ridge: Gas source implications., *Proc. ODP, Sci. Res., 164*: College Station, TX (Ocean Drilling Program), 67-78. https://doi.org/10.2973/odp.proc.sr.164.204.2000

Petersen, C. J., Bünz, S., Hustoft, S., Mienert, J., & Klaeschen, D. (2010). High-resolution P-Cable 3D seismic imaging of gas chimney structures in gas hydrated sediments of an Arctic sediment drift. *Marine and Petroleum Geology*, *27*(9), 1981–1994. https://doi.org/10.1016/j.marpetgeo.2010.06.006

Plaza-Faverola, A., Bünz, S., Johnson, J. E., Chand, S., Knies, J., Mienert, J., & Franek, P. (2015). Role of tectonic stress in seepage evolution along the gas hydrate-charged Vestnesa Ridge, Fram Strait. *Geophysical Research Letters*, *42*, 733–742. https://doi.org/10.1002/2014gl062474

Plaza-Faverola, A., & Keiding, M. (2019). Correlation between tectonic stress regimes and methane seepage on the western Svalbard margin. *Solid Earth*, *10*(1), 79–94. https://doi.org/10.5194/se-10-79-2019

Plaza-Faverola, A., Vadakkepuliyambatta, S., Hong, W.-L., Mienert, J., Bünz, S., Chand, S., & Greinert, J. (2017). Bottom-simulating reflector dynamics at Arctic thermogenic gas provinces: An example from Vestnesa Ridge, offshore west Svalbard. *Journal of Geophysical Research: Solid Earth*, *122*, 4089–4105. https://doi.org/10.1002/2016JB013761

Pohlman, J. W., Ruppel, C., Hutchinson, D. R., Downer, R., & Coffin, R. B. (2008). Assessing sulfate reduction and methane cycling in a high salinity pore water system in the northern Gulf of Mexico. *Marine and Petroleum Geology*, *25*(9), 942–951. https://doi.org/10.1016/j.marpetgeo.2008.01.016

Quigley, T. M., & Mackenzie, A. S. (1988). The temperatures of oil and gas formation in the sub-surface. *Nature*, *333*, 549. https://doi.org/10.1038/333549a0

Rice, D. D., & Claypool, G. E. (1981). Generation, accumulation, and resource potential of biogenic gas. *The American Association of Petroleum Geologists Bulletin*, *65*(1), 5–25.

Ritzmann, O., Jokat, W., Czuba, W., Guterch, A., Mjelde, R., & Nishimura, Y. (2004). A deep seismic transect from Hovgård Ridge to northwestern Svalbard across the continental-ocean transition: A sheared margin study. *Geophysical Journal International*, *157*(2), 683–702. https://doi.org/10.1111/j.1365-246X.2004.02204.x

Rivkina, E., Laurinavichius, K., McGrath, J., Tiedje, J., Shcherbakova, V., & Gilichinsky, D. (2004). Microbial life in permafrost. *Advances in Space Research*, *33*(8), 1215–1221. https://doi.org/10.1016/j.asr.2003.06.024

Ryan, W. B. F., Carbotte, S. M., Coplan, J. O., O'Hara, S., Melkonian, A., Arko, R., et al. (2009). Global multi-resolution topography synthesis. *Geochemistry, Geophysics, Geosystems*, *10*, Q03014. https://doi.org/10.1029/2008GC002332

Schneider, A., Panieri, G., Lepland, A., Consolaro, C., Crémière, A., Forwick, M., et al. (2018). Methane seepage at Vestnesa Ridge (NW Svalbard) since the Last Glacial Maximum. *Quaternary Science Reviews*, *193*, 98–117. https://doi.org/10.1016/j.quascirev.2018.06.006

Seeberg-Elverfeldt, J., Schlüter, M., Feseker, T., & Kölling, M. (2005). Rhizon sampling of porewaters near the sediment-water interface of aquatic systems. *Limnology and Oceanography: Methods*, *3*, 361–371. https://doi.org/10.4319/lom.2005.3.361

Seewald, J. S. (2003). Organic-inorganic interactions in petroleum-producing sedimentary basins. *Nature*, *426*(6964), 327–333. https://doi.org/10.1038/nature02132

Shipboard Scientific Party (1996), Site 986, *Proc. ODP, Init. Repts., 162*: College Station, TX (Ocean Drilling Program), 287-343. https://doi.org/10.2973/odp.proc.ir.162.109.1996

Sloan, E. D. (2003). Fundamental principles and applications of natural gas hydrates. *Nature*, *426*(6964), 353–363. https://doi.org/10.1038/nature02135

Smith, A. J., Mienert, J., Bünz, S., & Greinert, J. (2014). Thermogenic methane injection via bubble transport into the upper Arctic Ocean from the hydrate-charged Vestnesa Ridge, Svalbard. *Geochemistry, Geophysics, Geosystems*, *15*, 1945–1959. https://doi.org/10.1002/2013gc005179

Sommer, S., Pfannkuche, O., Linke, P., Luff, R., Greinert, J., Drews, M., et al. (2006). Efficiency of the benthic filter: Biological control of the emission of dissolved methane from sediments containing shallow gas hydrates at Hydrate Ridge. *Global Biogeochemical Cycles*, *20*, GB2019. https://doi.org/10.1029/2004GB002389

Stein, R., G. Brass, D. Graham, A. Pimmel, and the Shipboard Scientific Party (1995), Hydrocarbon measurements at Arctic Gateways sites (ODP Leg 151), *Proc. ODP, Init. Repts., 151*: College Station, TX (Ocean Drilling Program), 385-395. https://doi.org/10.2973/odp.proc.ir.151.112.1995

Sultan, N., Bohrmann, G., Ruffine, L., Pape, T., Riboulot, V., Colliat, J.-L., et al. (2014). Pockmark formation and evolution in deepwater Nigeria: Rapid hydrate growth versus slow hydrate dissolution. *Journal of Geophysical Research: Solid Earth*, *119*, 2679–2694. https://doi.org/10.1002/2013JB010546

Sztybor, K., & Rasmussen, T. L. (2017a). Diagenetic disturbances of marine sedimentary records from methane-influenced environments in the Fram Strait as indications of variation in seep intensity during the last 35 000 years. *Boreas*, *46*(2), 212–228. https://doi.org/10.1111/bor.12202

Sztybor, K., & Rasmussen, T. L. (2017b). Late glacial and deglacial palaeoceanographic changes at Vestnesa Ridge, Fram Strait: Methane seep versus non-seep environments. *Palaeogeography, Palaeoclimatology, Palaeoecology*, *476*, 77–89. https://doi.org/10.1016/j.palaeo.2017.04.001

Torres, M. E., Mix, A. C., & Rugh, W. D. (2005). Precise $\delta^{13}C$ analysis of dissolved inorganic carbon in natural waters using automated headspace sampling and continuous-flow mass spectrometry. *Limnology and Oceanography: Methods*, *3*, 349–360. https://doi.org/10.4319/lom.2005.3.349

Torres, M. E., Wallmann, K., Tréhu, A. M., Bohrmann, G., Borowski, W. S., & Tomaru, H. (2004). Gas hydrate growth, methane transport, and chloride enrichment at the southern summit of Hydrate Ridge, Cascadia margin off Oregon. *Earth and Planetary Science Letters*, *226*(1-2), 225–241. https://doi.org/10.1016/j.epsl.2004.07.029

Ussler, W. III, & Paull, C. K. (2008). Rates of anaerobic oxidation of methane and authigenic carbonate mineralization in methane-rich deep-sea sediments inferred from models and geochemical profiles. *Earth and Planetary Science Letters*, *266*(3-4), 271–287. https://doi.org/10.1016/j.epsl.2007.10.056

Valentine, D. L. (2011). Emerging topics in marine methane biogeochemistry. *Annual Review of Marine Science*, *3*(1), 147–171. https://doi.org/10.1146/annurev-marine-120709-142734

Vanneste, M., Guidard, S., & Mienert, J. (2005). Bottom-simulating reflections and geothermal gradients across the western Svalbard margin. *Terra Nova*, *17*(6), 510–516. https://doi.org/10.1111/j.1365-3121.2005.00643.x

Vogt, P. R., Crane, K., Sundvor, E., Max, M. D., & Pfirman, S. L. (1994). Methane-generated(?) pockmarks on young, thickly sedimented oceanic crust in the Arctic: Vestnesa ridge, Fram strait. *Geology*, *22*, 255–258. https://doi.org/10.1130/0091-7613(1994)022<0255:MGPOYT>2.3.CO;2

Vogt, P. R., Gardner, J., & Crane, K. (1999). The Norwegian-Barents-Svalbard (NBS) continental margin: Introducing a natural laboratory of mass wasting, hydrates, and ascent of sediment, pore water, and methane. *Geo-Marine Letters*, *19*(1-2), 2–21. https://doi.org/10.1007/s003670050088

Wallmann, K., Riedel, M., Hong, W.-L., Patton, H., Hubbard, A., Pape, T., et al. (2018). Gas hydrate dissociation off Svalbard induced by isostatic rebound rather than global warming. *Nature Communications*, *9*(1), 83. https://doi.org/10.1038/s41467-017-02550-9

Wei, J., Pape, T., Sultan, N., Colliat, J.-L., Himmler, T., Ruffine, L., et al. (2015). Gas hydrate distributions in sediments of pockmarks from the Nigerian margin – Results and interpretation from shallow drilling. *Marine and Petroleum Geology*, *59*, 359–370. https://doi.org/10.1016/j.marpetgeo.2014.09.013

Weinberger, J. L., Brown, K. M., & Long, P. E. (2005). Painting a picture of gas hydrate distribution with thermal images. *Geophysical Research Letters*, *32*, L04609. https://doi.org/10.1029/2004GL021437

Whiticar, M. J. (1999). Carbon and hydrogen isotope systematics of bacterial formation and oxidation of methane. *Chemical Geology*, *161*, 291–314. https://doi.org/10.1016/S0009-2541(99)00092-3

Whiticar, M. J., Faber, E., & Schoell, M. (1986). Biogenic methane formation in marine and freshwater environments: CO_2 reduction vs. acetate fermentation - isotope evidence. *Geochimica et Cosmochimica Acta*, *50*(5), 693–709. https://doi.org/10.1016/0016-7037(86)90346-7

Wilhelms, A., Larter, S. R., Head, I., Farrimond, P., di-Primio, R., & Zwach, C. (2001). Biodegradation of oil in uplifted basins prevented by deep-burial sterilization. *Nature*, *411*(6841), 1034–1037. https://doi.org/10.1038/35082535

Yao, H., Hong, W.-L., Panieri, G., Sauer, S., Torres, M. E., Lehmann, M. F., et al. (2019). Fracture-controlled fluid transport supports microbial methane-oxidizing communities at Vestnesa Ridge. *Biogeosciences*, *16*, 2221–2232. https://doi.org/10.5194/bg-16-2221-2019

References From the Supporting Information

Anderson, T. F., & Arthur, M. A. (1983). Stable isotopes of oxygen and carbon and their application to sedimentologic and paleoenvironmental problems. In M. A. Arthur, T. F. Anderson, I. R. Kaplan, & J. Veizer (Eds.), *Stable isotopes in sedimentary geology*, *The Society of Economic Paleontologists and Mineralogists (SEPM)*, (pp. 1-1–1-151).

Hong, W.-L., C. Schmidt, H. Yao, K. Wallmann, J. Rae, A. Lepland, et al. (2017). Fracture-induced fluid migration in an Arctic deep water pockmark: Porewater geochemistry from the MeBo drilling (MSM57) in Vestnesa Ridge (Svalbard), in Goldschmidt Abstracts, p. 1676, Paris.

Hyndman, R. D., Davis, E. E., & Wright, J. A. (1979). The measurement of marine geothermal heat flow by a multipenetration probe with digital acoustic telemetry and in situ thermal conductivity. *Marine Geophysical Researches*, *4*, 181–205. https://doi.org/10.1007/BF00286404

Myrvang, K. (2015). Correlation between changes in paleoceanography, paleoclimate and methane seepage on Vestnesa Ridge, eastern Fram Strait., 178 pp, University of Tromso, Norway.

Riedel, M., Wallmann, K., Berndt, C., Pape, T., Freudenthal, T., Bergenthal, M., et al. (2018). In situ temperature measurements at the Svalbard Continental Margin: Implications for gas hydrate dynamics. *Geochemistry, Geophysics, Geosystems*, *19*, 1165–1177. https://doi.org/10.1002/2017GC007288